NASA SP-8020

NASA SPACE VEHICLE DESIGN CRITERIA (ENVIRONMENT)

SURFACE MODELS OF MARS (1975)

REVISED
September 1975

NATIONAL AERONAUTICS AND SPACE ADMINISTRATION

FOREWORD

NASA experience has indicated a need for uniform criteria for the design of space vehicles. Accordingly, criteria have been developed in the following areas of technology:

Environment
Structures
Guidance and Control
Chemical Propulsion

Individual components of this work are issued as separate monographs as soon as they are completed. A list of all monographs published in this series can be found on the last pages of this monograph.

These monographs are to be regarded as guides to design and not as NASA requirements, except as may be specified in formal project specifications. It is expected, however, that the monographs will be used to develop requirements for specific projects and be cited as the applicable documents in mission studies, or in contracts for the design and development of space vehicle systems.

This revised monograph replaces an earlier version, Mars Surface Models (1968). The first draft of the revision was prepared under the cognizance of Marshall Space Flight Center. Subsequently, it was completed under the auspices of Goddard Space Flight Center. The principal author in both phases of the work was Dr. R. E. Hutton of TRW Systems; the program coordinator was S. A. Mills of Goddard Space Flight Center.

Comments concerning the technical content of these monographs will be welcomed by the National Aeronautics and Space Administration, Goddard Space Flight Center, Systems Reliability Directorate, Greenbelt, Maryland 20771.

September 1975

For sale by the National Technical Information Service
Springfield, Virginia 22161
Price - $4.75

CONTENTS

CONTENTS (cont.)

CONTENTS (cont.)

SURFACE MODELS OF MARS (1975)

1. INTRODUCTION

Engineering models of Martian surface properties are needed for mission planning and for the design of landing and exploration vehicles. Of paramount concern are those properties that have the greatest influence on landing safety. Typical properties of concern include local slope, roughness, and the mechanical properties of the soil at the touchdown site. The scientific objectives for a particular mission, however, may cause other surface properties to have equal importance in selection of a landing site. For example, if a primary mission objective includes the detection of biological life, mission planners must strive to select landing sites where biological life is most likely to be found. As a result, other items of paramount concern might include the abundance of water, variable features, atmospheric constituents or the thermal environment at candidate landing sites. For models of the Martian atmosphere to use in conjunction with this monograph, NASA SP-8010 (Revision of 1974) should be consulted.

Additional surface properties of interest include crater and block distribution because of their influence on landing safety and on the ability of a roving vehicle to move over the Martian surface. Atmospheric properties (such a pressure, density, and wind) are needed in designing a parachute landing system. Optical models are needed for the design of camera systems, and in the case of a manned landing, for assessing the capability of the crew to see landing site cues during approach, or to detect obstacles during the terminal landing phase. Additional surface models of interest include the dielectric and loss tangent needed in the design of radar systems and thermal properties needed in the design of the spacecraft thermal control system.

Although current knowledge of many of these surface properties is incomplete and uncertain, this monograph attempts to provide best estimates of engineering surface models based on 1974 state of the art. The monograph updates an earlier monograph (ref. 1) based on 1968 state of the art which reflected data obtained from Mariner 4. This version makes use of additional Mars information provided by Mariners 6, 7, and 9; Russian Mars probes; and photographic and radar observations conducted from Earth since 1968. When surface properties have not been observed or have not been measured for an area of the surface small enough to be related to vehicle surface operations, the available knowledge has been extended by means of Earth and Martian analogies. Such inferences are subject to the inherent uncertainty involved in the use of analogy.

2. STATE OF THE ART

Observations of Mars from Earth-based radar, high flying aircraft, rockets, and spacecraft have brought substantial advancements to man's understanding of Mars during the last decade. Instruments aboard Mariner spacecraft have provided scientific data from observations made near the planet. Television pictures transmitted from the Mariner spacecraft improved the surface resolution by orders of magnitude over that from the Earth-based

pictures which had resolutions to about 100 to 300 km (62 to 124 miles). A relatively close-up reconnaissance swath across the surface of Mars by Mariner 4 (1964-1965) at a minimum altitude of 9844 km (6118 miles) provided pictures of about one percent of the Martian surface. Mariners 6 and 7 (1969) also were flyby missions with Mariner 6 passing within 3341 km (2131 miles) and Mariner 7 passing within 3430 km (2130 miles) of the surface. Mariners 6 and 7 provided data covering about 20 percent of the surface. The best surface resolution obtained by Mariner 4, 6, and 7 pictures was about 300 m for the narrow angle and 3 km for the wide angle cameras.

Mariner 9 (1971), unlike the flyby missions of Mariners 4, 6, and 7, was placed in orbit about Mars with a periapsis altitude of about 1390 km (850 miles). The spacecraft provided data for almost a year and transmitted more than 7300 pictures which showed the entire planet at a resolution of about 1 to 3 km and about 1 to 2 percent of the planet at a resolution of 100 to 200 m. During the 1971 opposition, Russian probes (Mars 2 and 3) also provided data recorded from orbit about Mars.

Before the advent of space vehicles all knowledge of Mars was derived from Earth-based observations made by telescopes, radar, and radio telescopes. Such observations continue to advance man's understanding of Mars. Prior to 1969 Earth-based photographic studies of temporal changes in the atmosphere and surface features of the planets had been hindered by the discontinuous nature of the available data. This was particularly severe in the case of Mars because any single observatory sees essentially the same Martian face for several nights in succession. To avoid this difficulty, a cooperative program among eight observatories located around the Earth was established in 1969 and coordinated by the Planetary Research Center at Lowell Observatory where all photographs from the global network of observatories are processed and stored and available for study by qualified investigators (ref. 2).

2.1 Observation of Mars

Man's first understanding of Mars and its surface properties was deduced from Earth-based observations of the Sun's radiation after being reflected or reemitted from Mars. Over most of the electromagnetic spectrum, the Earth's atmosphere is opaque, or nearly so, and surface observations are only possible over certain wavelength ranges. The two most important windows occur in the visible band from about 0.4 to 0.8 μm and in the radio band from about 1 cm to 10 m. These radio band limits are set on the long wavelength side by ionospheric attenuation and on the short wavelength side by absorption in atmospheric gases.

Observations of radiation reaching Earth are made with a variety of instruments, each of which is responsive to portions of the total radiation spectrum received on Earth. For example, the determination of Martian surface temperatures is made from measurements that incorporate filters which pass energy in the wavelengths range 7 to 13 μm

Photometric observations are generally made over a wavelength band extending from the ultraviolet through the visual range and into the infrared. Such observations provide albedo

measurements over the planet disk that are sometimes interpreted in terms of properties of the surface material. Martian surface information is also deduced from a decomposition of the radiation into its spectrum by spectrophotometric techniques and by polarimetric techniques from the polarization of the sunlight after its reflection and emission from Mars.

Some conclusions deduced from Martian observational data have been found to be erroneous. For as Opik (ref. 3) points out, optical and radio observations of planets are often ambiguous and lead to contrary conclusions by different observers. One example cited to corroborate this contention concerns the 3.6 μm band in the infrared spectrum. The bands were originally attributed to heavy water on Mars but were later found to be caused by heavy water in the Earth's atmosphere.

2.1.1 Telescopic Methods

The best opportunities for telescopic observations of Mars occur at intervals of about 26 months when Earth and Mars are closest to one another (near opposition). The collection of photographic data showing details of the Martian surface is limited by the effective optical resolution of available telescopes. In large Earth-based telescopes, the resolution is usually limited by optical path differences caused by rapidly changing local irregularities in the Earth's atmosphere (called "seeing," ref. 4).

Until recently the study of large scale atmospheric changes and temporal changes in surface features was hampered by the lack of uninterrupted imaging showing day-to-day and hour-to-hour changes on Mars. The coordinated program established by the International Planetary Patrol Program in 1969 (ref. 2) now provides uninterrupted viewing of Mars during periods near opposition. Although these observations are not at a resolution afforded by spacecraft observations, they have the advantage that all faces of the planet are observed daily with only gradual changes in lighting and viewing angles. Such photographic data have permitted the detection of subtle changes in albedo or coloration that were missed in existing spacecraft observational data.

2.1.1.1 Areographic Observations

Since the invention of the telescope, astronomers have observed gross markings on the Martian surface. Because of uncertainties in the physical ephemeris elements, a comparison of the position of the same Martian features with different maps may show variations in the location of up to 600 km (ref. 5). For the small, apparently stable, dark areographic reference standard, such as the Juventae Fons feature with a dimension of 180 km by 120 km, the statistically refined location of its center was still in error by about 40 km. Because dark areas disappear at different times of the year (ref. 6), the location of the dark-bright area boundary had been most uncertain. An obscuring violet atmospheric layer caused additional difficulty in determining feature boundaries.

Improved Martian maps have been prepared at the Planetary Research Center, Lowell Observatory, with photographs obtained by the Planetary Patrol Program (ref. 7). Photographs obtained by Mariner 9 currently are being used to prepare vastly improved maps of Mars

(ref. 8). The photographs have a resolution limit some two orders of magnitude smaller than the best Earth-based telescopic photographs. Large-scale (1:5,000,000) maps prepared by the Astrogeology Branch of the United States Geological Survey (topography) and the Astronomy Department of the University of Texas (albedo) require commensurate improvement in the areographic coordinates to locate features on the surface of Mars. Maps distributed before 1972 were generally consistent with American Ephemeris system. Reference 8 describes a new Mars-centered system developed by the Geodesy-Cartography Group of the Mariner 9 Television Team proposed for future maps. The same reference reviews the original selection of the prime meridian (0° longitude) established in 1877 and its evolution over the years. The proposed prime meridian is close to the original prime meridian and is defined as passing through the center of about a 500 meter crater called "Airy-O" found within a large distinctive crater called "Airy." It is believed that the center of the crater (the prime meridian) will be defined within about 10 m.

Davies and Arthur (ref. 9) present results for primary and secondary triangulation of the Martian surface on the basis of Mariner 9 photography. A review of available Martian maps and those in preparation by the United States Geological Survey is given in reference 10. A preliminary albedo chart of the south polar region is given in reference 11 where the albedo markings range from about 0.03 to 0.04 for the dark spots to about 0.10 to 0.12 for the lightest areas.

2.1.1.2 Polarimetric Observations

Planetary polarimetry provides an independent source of compositional and micro-structural variations occurring on the surface of Mars. Extensive polarimetric investigations of Mars have been performed by Dollfus (refs. 12, 13, and 14) and Focas (ref. 6) who employed a Lyot polarimeter that allowed measurements of the degree of polarization from various bright and dark surfaces.

2.1.1.3 Photometric Observations

Many photometric experiments have been conducted to determine the surface albedo of Mars. The most quoted average spherical albedo for light of 5500 Angstroms wavelength is 0.159 (ref. 5). Often the reflected spectral pattern is interpreted in terms of composition of the surface material.

2.1.1.4 Radiometric Observations

Radiometric observations are generally obtained in the infrared or microwave spectral regions. Kellerman (ref. 15) points out there is an important difference between the infrared and radio techniques that are used to determine planetary temperatures. Infrared techniques generally use bolometers whose response is proportional to the total energy received and indicate surface temperatures that are insensitive to surface pressure gradients. Temperatures determined by radio wave techniques correspond to the temperature at depths below the surface that vary according to the electrical conductivity and the index of refraction of the surface material.

Earth-based measurements generally fall into two geometric categories; mean temperatures of the total planetary disk and temperatures of specific regions with dimensions in the order of 1/36 the planetary diameter. The best resolution has been better than 100 km which was provided by Mariner 9 (ref. 16).

2.1.1.5 Spectrophotometric Observations

The spectrum of reflected light from the Martian surface has been studied to deduce the chemical composition of the atmosphere and surface material. De Vaucouleurs (ref. 17) points out that the infrared bands of carbon dioxide near 1.6 and 2.0 μm were first detected by Kuiper in the infrared spectrum of Mars. Spectral data extending from the ultraviolet to the infrared region (0.3 to 4.0 μm) have been studied to determine Martian surface properties (ref. 18).

2.1.2 Radar Observations

In radar ranging the total time required for the radar signal to travel to and from Mars is measured. Variations in transit times are associated with differences in the radar path lengths which are assumed to show differences in Martian surface elevation after correction for the gross motion of the planet.

Radar observations give estimates along the subradar ground track of surface roughness in terms of the Root Mean Square (RMS) of the slope frequency distribution and surface elevation variations. RMS slopes are deduced from spectral width of the echo, whereas surface elevation variations are based on time delay measurements. Dielectric constants of the surface material are inferred from the radar cross section (related to reflectivity) which is obtained from the total power in the echo. The accuracy of the dielectric constant estimates is still very much an open question. More detailed discussions of radar observations and mathematical formulations are given in reference 20.

During each opposition since 1963, radar observations of Mars have been made by at least one among three groups in the United States and one group in the Soviet Union. The United States observatories (Goldstone, Haystack and Arecibo) provided measurements over the 3.8 to 70 cm range. During a night of observations, the ground radar track follows nearly a constant Martian latitude over a range of longitude that is a function of the observatory. Typical longitudinal coverages at Goldstone and Haystack encompass 100 degrees, the best at Haystack 180 degrees, and best at Arecibo 40 degrees. Variations of the ground track latitude during the oppositions of 1963, 1965, 1967, 1969, and 1971 are shown in figure 3 in reference 19.

References 21 through 29 tell of various studies of radar results from 1963 to 1973. References 30, 31, and 32 investigate possible correlations of dark and bright areas with altitude differences. It appears now that any apparent correlation among albedo, altitude, and radar behavior found in earlier studies may have been fortuitous. As radar data have become better, these correlation investigations seem to have been abandoned.

Recent topographic estimates from combined radar, Mariner 9 occultation, spectral, and optical results are given in section 2.3.9.1.

2.1.3 Martian Probes

2.1.3.1 Mariner 4

The Mariner 4 spacecraft flew within about 9850 km of the south pole surface in 1964. Primary objectives of the mission were to conduct a close-up television reconnaissance of Mars and to perform certain field and particle measurements in interplanetary space and in the immediate vicinity of the planet (refs. 33, 34, and 35).

The major scientific findings consisted of an indicated upper limit on the magnetic moment of Mars of 0.003 times that of Earth, a surface atmospheric pressure between 0.005 and 0.01 times that of Earth, and a cumulative crater distribution between that of the Lunar Maria and Uplands. In addition, the Martian craters were found to be more shallow than the lunar craters (refs. 33 and 34).

2.1.3.2 Mariners 6 and 7

Mariners 6 and 7 flew past Mars during the Mariner Mars 1969 mission with the following scientific experiments: (1) television, (2) infrared spectroscopy, (3) infrared radiometry, (4) ultraviolet spectroscopy, (5) S-band occultation, and (6) celestial mechanics.

The television experiment obtained data about crater sizes and slopes and other topographical information.

The infrared spectroscopy experiment obtained spectra data at wavelengths from 1.9 to 14.3 μm. These data were used to deduce surface topography, temperature, and the constituents and pressure of the Martian atmosphere.

The infrared radiometer experiment was designed to obtain radiation from the Mars surface by excluding atmospheric gaseous absorption from the Martian radiation. Pass bands in the two channels were 8.5 to 12.4 μm and 18 to 25 μm. Surface temperature measurements made by the instrument were at an areal scale about 10 times finer than obtainable from Earth.

The ultraviolet spectroscopy experiment measured emissions from the sunlit atmosphere above the limb of Mars over the wavelength range from 1100 to 4300 Å.

The S-band occultation experiment provided radio occultation data as each spacecraft moved behind Mars. The ingress and egress data were used to deduce the altitude, variation of atmospheric pressure, and temperature at the occultation points. Errors in the atmospheric properties determinations arose from uncertainties in the Mariner orbital paths, the nominal shape of Mars, and the composition of the Martian atmosphere (primarily the percent of CO_2).

Data provided by the celestial mechanics experiment were used to upgrade estimates of the Earth/Moon mass ratio and the product of the universal constant of gravitation G and the Martian mass M.

2.1.3.3 Mariner 9

Mariner 9 was placed in orbit about Mars during the Mariner-Mars 1971 mission to perform the same six scientific experiments conducted by Mariners 6 and 7. At the spacecraft's arrival on 14 November 1971, a planet-wide dust storm of unusual intensity was in progress. Although the storm delayed most planned experiments, it provided an unparalleled opportunity to examine the dust storm. The delay also allowed more scientific investigation of the Martian satellites Phobos and Deimos than planned.

On 22 September 1971 (before arrival of Mariner 9) Earth-based observers noted the development of a bright yellow cloud in the midsouthern latitudes of Mars over Noachis. In a little more than two weeks the cloud spread over the rest of the planet. Television pictures taken by Mariner 9 from an orbit with a periapsis altitude of 1387 km verified the planet-wide obscuration which was confirmed by the infrared spectroscopy, infrared radiometry, ultraviolet spectrometer experiment, and the S-band occultation experiments.

Data from Mariner 9 experiments showed that the surface of Mars is geochemically differentiated (ref. 36) and has extensive volcanic terrains. The surface was found heavily cratered in places, considerably eroded and blanketed by aeolian sediment, and locally eroded by water. Mariner 9 data have been the primary source for the upgraded surface models presented here.

2.1.3.4 Mars 2 and 3

During 1971 Mars 2 and 3 were launched by the USSR and placed in orbit at periapsis altitudes of 1380 and 1530 km. Mars 3 also had a lander stage which separated from the orbiter stage and made a soft landing. Signals from the lander suddenly terminated 20 seconds after landing, thereby eliminating the possibility of transmitting data from the surface. The Mars 2 and 3 orbiters carried optical and radio instruments to study the surface and lower atmosphere. Instruments included an infrared radiometer for measuring brightness temperatures in the 8 to 40 μm wavelength range, a 3.37 cm microwave radiometer for measuring radio emissions from Mars to determine the temperature and dielectric constant of the top 30 to 50 cm of the surface, an infrared photometer to determine surface elevations from the absorption intensity of CO_2, an infrared polarized photometer for the determination of water vapor content along the optical path and a photometer to measure the brightness distributions of the surface and atmosphere in five narrow spectral ranges in the visible zone of the spectrum from 0.36 to 0.60 μm, a four channel ultraviolet photometer to measure diffuse ultraviolet radiation in the upper atmosphere of Mars, and two television cameras having 26° and 5°40′ field of views.

2.2 Physical Properties of a Spherical Mars

Many of the quantitative descriptions of Martian physical properties have not been changed significantly by spacecraft explorations conducted thus far. The method for their determination and the values presented in this monograph are taken mainly from Michaux and Newburn (ref. 19). Nominal properties for homogeneous spherical Mars including average radius, average mass density, escape velocity, nominal gravitational acceleration, and other parameters are presented in section 3.1.

2.3 Surface Properties

2.3.1 Atmosphere

NASA SP-8010 (Models of the Mars Atmosphere (1974), Revision of December 1974) gives atmospheric parameters from the surface upward.

2.3.1.1 Composition

Observations of haze and clouds surrounding Mars for the past century and a half provided ample evidence of the existence of a Martian atmosphere. Further evidence is provided in comparisons of photographs taken in red and blue light. The red rays penetrate the Martian atmosphere and reveal surface markings. Photographs taken in blue and violet light generally show a featureless surface except for a bright cap at the pole. The blue photographs primarily show the outer atmospheric shell surrounding the planet. Occasionally, the atmosphere clears and photographs taken with blue or violet filters show almost as much detail as with red filters (ref. 31). Such rare occasions are called blue clearings.

Spectroscopic studies of Mars over more than 80 years have provided upper limits on the abundance of constituent gases but gave no conclusive evidence on composition. In 1946, however, comparisons of infrared spectrum of sunlight reflected from the Moon with that from Mars led Kuiper to conclude that carbon dioxide was present (ref. 31). In 1963 L. D. Kaplan, G. Munch, and H. Spinrad obtained spectroscopic proof that water vapor existed in the Martian atmosphere (ref. 31).

The infrared spectrometers on Mariners 6 and 7 gave information on overall atmospheric abundances (ref. 37) and established CO_2, CO, and H_2O as three of the constituents. Data from the S-band occultation experiment were reduced by assuming the Martian atmosphere contained 90 percent carbon dioxide. Data obtained by Mars 2 and 3, however, led the Soviets to conclude that 30 to 40% of the atmosphere may be argon. This order of abundance for argon or some other inert gas is considered reasonable by Viking Project members.

Owen and Sagan (ref. 38) give estimates of the minor constituents of the Martian atmosphere which were deduced from ultraviolet spectroscopy data from the Orbiting Astronomical Observatory. The data faintly indicated atmospheric structure in the 3200 to 3600 Angstrom region, but there was no convincing evidence of absorption anywhere in the spectrum. The data were reported to be consistent with a pure Rayleigh atmosphere of carbon dioxide at a surface pressure of about 5.5 mb.

2.3.1.2 Temperature

Temperature profiles are deduced from the Mariner 9 infrared spectroscopy experiment in reference 39 which gives curves that show the relationship among pressure, temperature, and altitude for the 667 cm^{-1} (50 μm) CO_2 absorption band with a pure CO_2 atmosphere.

Profiles are shown for the Hellas, Sinai, and the south polar regions. Additional temperature profiles for the polar regions that are deduced by Conrath et al. from the 667 cm^{-1} (50 μm) CO_2 absorption band are presented in reference 40. Also shown on the profiles are surface temperatures derived from the 400 cm^{-1} (25 μm) region of the spectrum. The results indicate the T_{25} temperatures (25 μm band) are generally lower than the T_{50} temperatures (50 μm band). For example, in the south polar region the surface brightness temperatures T_{25} and T_{50} were 155°K and about 185°K, respectively

2.3.1.3 Water Content

The two theories concerning the polar caps, the ice cap theory and the dry ice theory, were investigated in reference 41. The earlier ice cap theory held that the polar caps were similar to the Arctic ice fields on Earth. Subsequently, Mariner 4 data indicated the surface pressure to be about 10 mb (much lower than earlier estimates) and that the principal component of the atmosphere was CO_2. This strongly supported the dry ice theory because ground temperatures associated with the lower surface pressure were estimated to drop below the freezing point of CO_2 (146.4°K). However, Miyamoto and Hattori (ref. 41) reported in 1968 that the dark wave and cloud distribution seems to fit the old ice cap theory better. By taking into account the greenhouse effect of water vapor, they concluded that the ground temperature was above the freezing point of CO_2 even in the winter polar region. They proposed that water vapor (a minor constituent of the atmosphere) was an important agent which gave rise to air currents through the absorption of long wave radiation. Wade and De Wys (ref. 42) discuss the possible presence of CO_2 and H_2O in the liquid, solid, or vapor phases according to the type of Martian topographic features. Observations of Mars in 1969 at the McDonald Observatory provided high-resolution spectra that confirmed the existence of water vapor in the atmosphere (ref. 43).

The most definitive water vapor information has been provided by the Mariner 9 Infrared Spectroscopy Experiment (IRIS) which gave conclusive evidence of the existence of water vapor in the Martian atmosphere (refs. 40 and 44). The IRIS instrument measures radiation that originates from the surface and from atmospheric gases and aerosols. From these thermal emission data, surface and atmospheric temperatures, composition, and total CO_2 in the atmospheric column are retrieved if the spectral resolution is less than 5 cm^{-1} to permit the detection of details in the contours of gaseous absorption bands.

IRIS data showed numerous rotational lines of water vapor throughout the range from 250 to 500 cm^{-1}. Strong seasonal variations in water vapor distribution were detected over both polar caps. The highest vapor content was 20 to 30 precipitable μm over the north polar cap during northern spring. A slight decrease occurred as the entrained dust settled during the final stages of the dust storm, probably because of water vapor absorbed by the suspended dust. Then, with increasing surface temperatures some of the water vapor absorbed by the dust would be returned to the atmosphere. IRIS data recorded over Tharsis Ridge agreed best with theoretical spectra that were based on water ice clouds composed of particles with a mean radius of 2.0 μm and an integrated cloud mass of 5×10^{-5} g/cm^2 (ref. 45).

Evidence of bound water was also shown in the reflectivity measurements made in the 2.0 to 4.0 μm band from high flying aircraft in 1971 (ref. 46). At the altitudes 11.6 to 12.5 km

where the reflectivity measurements were made, the atmosphere has lose to 100 percent transmission over the 2 to 4 μm range. The data showed a broad absorption band with a minimum at 2.85 μm; this led to an estimate of bound water content of approximately 1 percent by weight with an uncertainty factor of about 3. This estimate was considered consistent with the volcanic features photographed from Mariner 9 and with observation of the silicate infrared reststrahlen features in the Mariner 9 Infrared Spectroscopy Experiment.

Leovy et al. (ref. 47) suggest that clouds 5 to 10 km above the caldera floor of Arsia Mons (observed by Mariner 9) were composed of water ice. Milton (ref. 48) proposes that running water has been a principal agent of Martian surface erosion some time in the past; this would explain the large channel features, notably bars and braiding. Other proposed eroding agents are liquid or solid CO_2, lava flows, wind erosion, and tectonic fracturing (refs. 49, 50, and 51).

2.3.2 Clouds

Early telescopic observations of Mars revealed transient changes in Martian features that were interpreted as clouds. The clouds were classified according to their color: white, blue-white, blue, and yellow (ref. 31). The color actually represents the part of the sunlight reflected by the cloud; this is best determined with the aid of color filters.

Reference 52 gives results from a study of bright features in telescopic photographs taken in blue light which show diffuse and discrete bright features superimposed upon a relatively dark disk. The bright features are characterized as Type I and Type II clouds. Type I clouds are a diffuse brightening usually seen near the terminator in the equatorial and temperate regions; Type II clouds are not associated with any particular surface location. Type II clouds are described as discrete features having quasi-stable locations. Activity of both types varies with season. Type I clouds also vary diurnally. The brightening begins in the late morning or early afternoon and continues for several hours until the clouds passed over the evening terminator; however, the clouds do not reappear over the morning terminator. Type II clouds do not vary diurnally; when active, they are bright from their first appearance over the morning terminator until their disappearance across the evening terminator. It was concluded that Type I clouds are actual clouds composed of water ice. Type II features are believed to be CO_2 condensation, most probably in the form of a frost deposit.

In reference 53, Baum reports on transient cloud data obtained from the Planetary Patrol Program. Data show transient brightenings that have been detected by red, green, blue, and ultraviolet photographs on all sides of the planet. In a few places the frequent appearance of white clouds correlates with prominent topographical features such as the western slopes of Olympus Mons. Investigations by Sagan et al. (ref. 54) also indicated a correlation of white cloud frequency with elevation, probably because of adiabatic cooling of rising air. White streaks near Olympus Mons follow topographic contour lines which may be aeolian deposits of fine surface material.

The yellow clouds observed on Mars before Mariner 9 were generally accepted as being very fine particles of surface material that have been carried aloft by the wind (ref. 31). Yellow

clouds or storms with linear dimensions from 400 to 2000 km have been observed approximately once per year moving across the planet with an average speed of 40 km/hr. Some observers indicated speeds as high as 100 km/hr.

Spectral data obtained by the Mariner 9 IRIS experiment show features that are characteristic of silicate materials and yield an estimated SiO_2 content of 60 ± 10 percent for the dust in the Martian clouds (ref. 44).

Yellow clouds appear as a transient brightening of light areas according to Baum (ref. 53). Historically, this phenomenon has been confusingly associated with terms like "blue clearing" or "violet haze," but photographic and photoelectric data indicate the color associated with these brightness changes to be yellow. This phenomenon clearly implied a chronic dust activity in the light areas. According to Boyce and Thompson (ref. 55), the development of the yellow cloud is compatible with the concept that the stirring of dust is related to the amount of solar heating.

In reference 56 Boyce reports that the light areas surrounding Nilokeras and Syrtis Major had an increase in albedo of about 8 percent between 10 a.m. and 2 p.m. each Martian day during 1969. He added that Baum attributed the albedo variation to the daily raising of dust particles in a 100 m layer above the surface which settled out during the night.

2.3.3 Surface Winds

2.3.3.1 Velocities

Estimates of surface wind velocities and the relation of wind velocity to the erosion of the surface material has occupied the attention of many investigators for several years. Conclusions reached by the investigators ranged from low velocity winds which cause little or no surface erosion to high velocity winds which cause extensive surface erosion. Because Mariner 9 provided conclusive evidence of a global dust storm and obtained photographs after the storm of regions similar to large-scale deserts on Earth, there is general agreement of Martian aeolian processes.

Theoretical wind velocity estimates are generally made from observations of cloud movements. Blumsack (ref. 57) developed a theoretical model to study steady winds as influenced by large-scale topography and the associated large-scale atmospheric circulation caused by thermal and dynamic effects. He quotes other investigators who indicate the average velocity of clouds to be in the range 8 to 45 m/s. In reference 58, Gifford gives results from a study of yellow cloud motions and discusses Bagnold's theory (ref. 59) concerning wind induced sand motion. Gifford estimates the average drift velocity of the yellow clouds to be about 8 m/s with associated winds that have velocities large enough to move soil particles. The yellow clouds are most likely composed of wind-driven sand grains that are moved by saltation within a few meters of the Martian surface and are accompanied by an overlying dust cloud of much smaller particles which extends to many thousands of meters.

The estimate of Gierach and Sagan (ref. 60) that elevation differences on Mars are on the order of the atmospheric scale height leads them to conclude that topographic relief could increase the mean wind velocities in local areas by a factor of 2 to 3.

For maximum steady wind velocities, reference 61 gives an estimate of 70 m/s above the surface layer of blowing sand grains and 40 m/s within the surface layer at about one meter elevation. References 62 and 63 deduced estimates of maximum velocities from 100 to 145 m/s on the basis of theoretical computations made by Leovy and Mintz. Reference 61 holds that surface gusts should be assumed to have a 3σ value equal to one-half the maximum free stream velocity, i.e., 35 m/s, and that combined steady wind and gusts should not be considered to exceed 70 m/s.

2.3.3.2 Dust Storms

A short review of Martian dust storms since 1892 is given by Golitsyn (ref. 64). Dust storms of great intensity and global scale have been observed only at times of favorable opposition.

Koval (ref. 62) estimated the total mass of dust particles in the atmosphere during the 1971 dust storm to be on the order of 10^9 tons. Because of this large amount, he favored the dust hypothesis over the vegetation and micro-organisms hypothesis for explaining the observed transient phenomenon that has been called the wave of darkening.* For further discussions of the wave of darkening, see Glasstone (ref. 31), Pollack and Sagan (ref. 65), Otterman and Bronner (ref. 66), Richardson and Bonestell (ref. 67), and Martin.**

Local dust storms are described by some investigators as being initiated by saltation or by dust devils (refs. 58 and 68). Sagan and Pollack (ref. 68) estimate the Bagnold drag velocity parameter V_* (ref. 59) must be at least 4 m/s to initiate removal of 400 μm diameter particles from the surface at a 5 mb pressure. They indicate the parameter V_* is about 2 to 5 percent of the wind velocity along the surface just above the boundary layer. In reference 64, Golitsyn estimated the average value of V_* to be only about 1/4 to 1/2 the threshold value required to initiate saltation but suggested that Martian conditions may cause local increases in V_* sufficient to exceed the erosion threshold value. In 1968 Sharp (ref. 69) concluded that wind and thermal creep were the most promising processes for explaining differences between lunar upland craters and the Martian craters seen in the Mariner 4 pictures. He doubted that wind had eroded the surface extensively because high wind velocity apparently is required for significant aeolian action on Mars. He used estimated requirements for wind velocities from 72 to 96 m/s to pick up soil from the Martian surface. Yet other investigators indicate clouds only have average velocities in the range 8 to 45 m/s.

An indication of the free stream velocity required to initiate soil motion under Martian type atmospheric conditions is provided by the experimental results presented in reference 70

*W. A. Baum, "Earth-Based Observations of Martian Albedo Changes," ICARUS, vol. 22, 1974, pp. 363-370, points out that calibrated photometry has established that these seasonal variations of contrast result from a brightening of light areas rather than darkening of dark areas. The latitude of maximum contrast approximately follows the Sun and is now believed to be caused by a midday raising of dust near the surface at the latitude of maximum insolation.

**L. J. Martin, "The Major Martian Yellow Storm of 1971," ICARUS, vol. 22, 1974, pp. 1[illegible]-188.

which discusses tests at wind speeds up to 76 m/s over static pressures from 5.3 to 9.3 mb. In the tests it was found that 297 to 420 μm diameter silica sand particles with a bulk density of 1.5 g/cm^3 began to roll along the surface at wind speeds of 54.9 m/s. Particles began to lift from the surface and start a saltation type motion at a wind speed of 74.9 m/s. If one assumes the resistive force preventing the particles from moving is proportional to the gravity force and the force tending to move the particles is proportional to the dynamic wind pressure, then the corresponding velocities in the Martian gravity field would be reduced by the square root of the gravity ratio. In that event one would estimate particles to begin moving and to begin a saltation motion at free stream wind velocities of 34 and 46 m/s, respectively.

Test data presented in reference 71 indicated free stream velocities required to initiate a saltation motion in a Martian gravity field should be about 50 and 59 m/s for particles ranging from 1 to 210 μm in diameter. This is approximately the same as the 50 to 60 m/s range estimated by Wood et al. in reference 72 and contrasts with the estimate of 110 m/s for initiating sand or dust motion over a flat surface by Greeley et al. in reference 73.

Although the tests in references 70 and 71 may not have simulated the boundary layer flow over the Martian surface, the results imply surface erosion should occur at free stream wind velocities less than the upper bound value of 70 m/s in reference 61, and therefore are compatible with the occurrence of dust storms on Mars.

2.3.4 Surface Pressure

Photometric and polarimetric methods (ref. 31) were used to estimate the Martian surface atmospheric pressure prior to 1963. In the photometric method atmospheric pressure is deduced from variations of brightness of the planet at different wavelengths and phase angles Apparent brightness arises from scattering of sunlight by surface material and by atmosphere. The scattering contribution from the atmosphere is used to determine surface pressure from established formulas that relate gas pressure and brightness caused by scattering.

In the polarimetric method, the light scattered by the surface is determined from polarization measurements on various Martian soil simulants. By subtracting the surface polarization contribution from the total polarization one obtains the polarization contribution from the atmosphere. Relations between atmospheric polarization and barometric pressure are then used to estimate surface pressure. For many years the surface pressure was believed to be about 80 mb mainly on the basis of polarimetric data obtained by Dollfus (ref. 74).

In 1963 observations of the infrared spectrum of carbon dioxide indicated the earlier surface pressure estimates were high by about a factor of 4 or more. In 1964 and 1965 reflectivity measurements were made in the ultraviolet region of the spectrum where light scattered from the surface is essentially zero. Measurements made by de Vaucouleurs at a wavelength of 3300 Angstroms indicated a surface pressure of 19 mb for an atmosphere consisting entirely of carbon dioxide. Evans, on the other hand, based his calculations on measurements of reflectivity made from a rocket above Earth's tangible atmosphere in the

wavelength range 2400 to 3500 Angstroms. His results agreed with surface pressures ranging from 5 to 20 mb for atmospheres consisting of various mixtures of carbon dioxide, nitrogen, and argon.

Ground based polarimetric data taken over the wavelength range 0.32 to 0.70 μm by Ingersoll indicated surface pressures from 4 to 7.5 mb if CO_2 is the principal constituent (ref. 75). This pressure range is in agreement with those deduced from occultation data.

The Mariner 4 spacecraft provided the first data obtained from the vicinity of Mars for estimating surface pressure. Measurements of the refraction of the radio signals just before and after occultation as Mariner 4 passed behind Mars were used to deduce surface pressures. The estimates for an atmosphere composed entirely of carbon dioxide ranged from a minimum of 4.1 mb before occultation to a maximum of 9.7 mb after occultation (ref. 31).

Pressures estimated from the occultation data obtained from Mariners 6 and 7 were approximately the same as from Mariner 4 data. Three of the four pressure estimates were in the range between 6 and 7 mb (ref. 76).

Reference 40 gives surface pressures derived from more than 3500 infrared spectroscopic measurements by Mariner 9. These data were averaged to provide a low-resolution pressure map of the planet between latitudes $-60°$ and $25°$. The average surface pressures over the sampled area was 4.8 mb. Correlation of surface pressure data with topographic features was clearly evident. Highest pressures occurred in the Hellas and Isidis Regio-Amenthes areas and were about 8 mb. The lowest surface pressure was about 1.5 mb at the top of Arsia Mons. Reference 77 presented additional surface pressures based on Mariner 9 S-band occultation data.

Reference 78 compares surface pressures which were determined from occultation experiments on Mariners 4, 6, 7, and 9. The entry occultation values generally lie below those from exit occultation data. Interpolations indicate the surface pressure at zero elevation is about 6 mb for the entry data and 7.3 mb for the exit data. The higher exit pressures most likely result from the smaller planetary radius at exit locations. Another interpretation is that the exit values are higher because night-time conditions are being measured rather than the day-time conditions from entry. One explanation is the possible presence of a low-lying electron layer on the day side that would tend to reduce pressure (ref. 78).

2.3.5 Thermal Properties

2.3.5.1 Temperature

Theoretical estimates of the nominal Martian surface temperature at the subsolar point are readily made by assuming the planet to be in temperature equilibrium with its surroundings and radiating energy as an ideal blackbody. At the average distance from the Sun, Mars receives energy at the rate of 0.66 cal/cm^2/min (ref. 31). Setting this rate equal to the theoretical radiation rate expressed by the Stefan-Boltzmann equation

$$E = 8.28 \times 10^{-11}\ T^4\ \text{cal/cm}^2/\text{min}$$

and solving for the temperature T gives T = 299 K. At perihelion when the planet is closer to the Sun, the temperature at the subsolar point would be about 15 K higher.

Theoretical estimates of the average surface temperature have been made by assuming Mars absorbs solar radiation only on the area of the planet facing the Sun (πR^2) and radiates energy from the entire surface area of the planet ($4\pi R^2$). By taking the maximum temperature to be that at the subsolar point, the average temperature is estimated to be $\sqrt{2}$ smaller, or for T_{max} equal to 299 K; the average temperature of the surface should be 211 K. At perihelion it would be about 10 K higher and at aphelion about 10 K lower.

The first estimates of surface temperatures came from Martian radiation as measured on Earth. This consists of reflected or scattered sunlight plus thermal radiation from the Martian surface. The thermal radiation must be extrapolated from the observed total radiation before it can be used to derive surface temperature. The first radiation measurements were made during 1922, 1924, and 1925, but the derived temperature estimates were susceptible to considerable error because of inadequate data (ref. 31).

Improved methods used by Sinton and Strong in 1960 (ref. 79) incorporated filters to restrict the radiation energy received from the planet to the infrared range of 7 to 13 μm, which is essentially the range of emission from the surface. These data indicated the maximum temperature at the equator is close to 300 K and is reached about an hour after local noon. The estimated temperature at the same point drops to a minimum value of about 190 K during the night. The large daily temperature variation of about 110 K is a result of the low atmospheric density and poor thermal conductivity of the surface material (ref. 31).

Between 1926 and 1943, Lampland conducted a systematic program of Martian radiometry. His results were analyzed by Gifford (ref. 80) to delineate the broader features of the surface temperature distribution.

A modification of the infrared radiometric method was utilized by C. H. Mayer and his coworkers at the U.S. Naval Observatory during the 1956 and 1958 apparitions by which temperature was determined from radiation emitted at longer wavelengths (3.15 cm) (ref. 81). The resulting temperature estimates were significantly lower (about 210 K) than the mean infrared daytime temperature (about 250 K) over the entire disk. An explanation is that longer wavelength radiation originates from a short distance below the surface where the temperatures are a little cooler than the surface from which the shorter wavelength infrared radiation originates (ref. 31).

Kellerman (ref. 15) measured the thermal radiation from Mars at 6, 11, and 21 cm wavelengths with a 210 ft radio telescope. A comparison of these brightness temperatures with those determined by other investigators at radio and infrared wavelengths also indicated the temperatures deduced by radio wave techniques to be a little cooler. Measurements made at 0.822 cm by Kuzmin et al. (ref. 82) led them to conclude the thermal wave penetrates 1.8 to 3 cm and 50 to 80 cm into the surface during the diurnal and seasonal variations, respectively.

Reports of brightness temperature measurements by other investigators are given in references 83, 84, 85, and 86. The problem of how brightness temperature varies with radio wavelengths that are used to obtain data was not resolved but receives considerable attention in references 87, 88, 89, and 90.

More recently, brightness temperatures have been deduced from Mariner 9 infrared radiometric measurements at 10 and 20 μm wavelengths for more than 34 percent of the surface with some areas observed at a spatial resolution as small as 15 km (ref. 16). During the earlier Mariner-Mars 1969 mission, approximately 2 percent of the Martian surface had been observed by radiometers with a linear resolution of 50 km, at best.

According to Mariner 9 data, the gross thermal characteristics (after the 1971 dust storm subsided) agreed qualitatively with the lower resolution data obtained during the Mariner-Mars 1969 mission. At the height of the storm the average daytime temperatures of the planet were about 20 K lower than after the storm. Mariner 9 brightness temperature contours are given in reference 16.

Radiometric data obtained by Mariner 9 were also examined to investigate possible regional differences in Martian thermal properties. Thermal differences were observed between light and dark areas, regions of large and small albedo, and regions of high and low elevations. The data indicated thermal similarity among the three heavily-cratered areas that were studied despite their striking differences in visual albedo.

Mariner 9 data were also examined to determine whether local thermal deviations from the mean background could be associated with features observed by the television cameras. The comparison indicated a small-scale correlation between temperature and visual albedo. An anomalously warm area near the southern boundary of Elysium was also detected by the radiometer aboard the USSR Mars 2 probe (ref. 16) and Mars 3 data showed other localities to be about 10 degrees warmer than surrounding areas (ref. 61). Several cool areas observed during the daylight hours by the Mariner 9 radiometer were identified in the television pictures as clouds. Other cold anomalies were found to be associated with impact craters having bright areas on their floors. The temperatures were generally higher than appropriate for Martian frosts so the low temperatures may result from local or thermal albedo variations.

Temperature profiles deduced from Mariner 9 S-band occultation data indicated the near-surface daytime temperatures on the north polar cap in the Martian spring range 180 to 190 K (ref. 77). Measurements near the south pole indicated temperatures close to the condensation temperature of CO_2 (about 140 K at 5 mb pressure). Surface temperatures measured between latitudes 30°S and 30°N had maximum and minimum values of 235 and 141 K with an average value of about 200 K. These temperatures are a little lower than the 10 μm brightness temperature profiles shown in reference 16.

Kieffer (ref. 91) utilized available Martian temperature data to develop a theoretical model for predicting Martian surface and near surface temperatures over the entire planet for all seasons. This work was used to develop the temperature models for this monograph (section 3.8.1).

2.3.5.2 Thermal Inertia

Values of the thermal inertia $I = (k\rho c)^{1/2}$ were deduced from radiometric data obtained over wavelengths from 8 to 13 μm by Sinton (ref. 79). A comparison of theoretical diurnal temperature variations with observed variations indicated no single choice of thermal inertia that provided agreement both in amplitude and phase simultaneously. It was found that a milli-inertia* value of 10 provided the best agreement in amplitude, while a value of 4 provided the best agreement in phase lag. Morrison (ref. 92) also used Sinton's radiometric data and concluded that measured temperatures were consistent with his theoretical computations with a milli-inertia value of 5. Milli-inertia values used by other investigators were 7.5 ± 3.5 by Efanov and Troitskii (refs. 82 and 83) and 11 by Gifford (according to Leovy, ref. 93). Kuzim et al (ref. 82) used the values 4 and 10 and found that $I = 4$ (10^{-3} cal/cm^2 s$^{1/2}$ K) fitted the data better.

Kieffer (ref. 16) notes the value mI = 6 from Mariner 6 and 7 data adequately represents the average thermal structure of Mars obtained from Mariner 9 data. He adds that values as low as 10 are required for theoretical results to agree with the measurements in some regions, especially in Hellas. Values of 8 and 6 for mI agreed with Mars brightness temperature measurements made after the 1971 dust storms by Mars 2 and 3 (refs. 94, 95, and 96). During the storm, values between 5 and 8 failed to give good agreement with brightness temperature measurements. This disagreement was believed to be due to the greater opacity of the dust particles in the cloud to solar radiation in the visible wavelength range rather than to heat loss.

It might be of interest to compare these mI values with those recommended for the lunar surface for the temperature range 125 to 375 K in reference 97. The mI values for the lunar regolith were from 0.6 to 1.1 (900 to 1600 cm^2 s$^{1/2}$ K/cal) and for the lunar rocks were from 29 to 50 (20 to 35 cm^2 s$^{1/2}$ K/cal). The mI range of values for the Martian soil given in section 3.8.3 of 4 to 10 (10^{-3} cal/cm^2 s$^{1/2}$ K) is selected on the basis that the range gives satisfactory agreement with Mariner 9 and other data.

2.3.5.3 Thermal Conductivity

Reference 98 gives results from thermal conductivity measurements made on 37 to 62 μm diameter basalt powders in lunar and Martian simulated environments The samples were tested at packing densities ranging from 0.79 to 1.50 g/cm^3 in simulated Martian atmospheres using CO_2 at 7 mb pressure at temperatures ranging from about 200 to 300 K. The thermal conductivity was found to be essentially independent of packing density and temperature. Evidently the interstitial CO_2 tends to negate the effects of temperature and density. The thermal conductivity measurements in the Martian environment ranged from about 0.23×10^{-4} to 0.29×10^{-4} cal/cm s K. In the simulated lunar vacuum and temperature regime the thermal conductivity was found to increase with density. It also increased with temperature approximately according to the law $k = A + BT^3$ where A and B are constants. Because the Martian temperature is lower than the lunar temperature, some

*One milli-inertia unit (mI) is equal to 10^{-3} cal/cm^2 s$^{1/2}$ K.

investigators believe the BT^3 term is small enough compared to the A term that the thermal conductivity of the surface can be considered independent of temperature.

There are no direct measurements of thermal conductivity of the Martian surface material. Current estimates are made from the measured thermal inertia by using representative values for the specific heat and density of the Martian surface material. Data compiled by Winter and Sarri (ref. 99) for most common geologic materials suggest the specific heat lies in the range 0.10 to 0.18 cal/g K over the Martian temperature range (150 to 300 K). From these data Kieffer concluded that 0.16 is a reasonable average value for the specific heat and 0.3 cal/cm^3 K is a reasonable value for the product of soil density and specific heat (ρc). Accordingly, for a measured thermal inertia of 6×10^{-3} cal/cm^2 s$^{1/2}$ K, the thermal conductivity would be 1.2×10^{-5} cal/cm s K corresponding to the value $\rho c = 0.3$ cal/cm^3 K.

These results led to the thermal conductivity range recommended in section 3.8.3. This range encompasses values used by other investigators in their analysis of Martian data, i.e., in units of cal/cm s K, 1.0×10^{-4} and 1.6×10^{-4} by Leovy (ref. 93), $(7 \pm 3) \times 10^{-5}$ and $(12 \pm 4) \times 10^{-5}$ by Morrison et al. (ref. 92), and 1×10^{-4} to 7×10^{-4} by Troitskii (ref. 100). Kieffer et al. in reference 16 used the values 10^{-5} to 10^{-3} cal/cm s K measured on powdered rocks having diameters ranging from 40 to 800 μm. The thermal conductivity measured in situ on the lunar soil was 0.33×10^{-4} cal/cm^2 s K at a 49 cm depth and 0.60×10^{-4} cal/cm s K at a 138 cm depth (ref. 97).

2.3.5.4 Specific Heat

Typical specific heat values c used by investigators during their analysis of Martian data (in units of cal/g K) have been 0.17 (refs. 83, 88, and 100), 0.15 (ref. 93), and 0.19 (ref. 101). The specific heat recommended for lunar rocks or lunar soil in reference 97 ranged from 0.06 to 0.20 over the temperature range from 100 to 370 K. These values and the range 0.10 to 0.18 measured on most common geological materials (ref. 99) formed the basis for the range recommended in section 3.8.3.

2.3.5.5 Emissivity

Infrared reflectance measurements made on several terrestrial rocks and other materials by Hovis and Callahan (ref. 102) have been used for estimating emissivity of the Martian surface material. From these data Kieffer and his coworkers have adopted a value of about 0.95 in their thermal investigations of the Martian soil. Emissivity values adopted by other investigators include 0.85 (ref. 101) and 0.90 (ref. 93). Recommended values for the Martian soil in section 3.8.3 are 0.90 to 0.98. These values are a little higher than the values 0.8 and 0.6 recommended earlier for the bright and dark areas in reference 1.

2.3.6 Gravitational Field

First estimates of the average gravitational acceleration at the surface of Mars were obtained from the equation $g = GM/R^2$ for a spherical planet where G is the universal constant of

gravitation (6.67×10^{-8} $cm^3/g\ s^2$), M is the mass, and R the radius. Reference 31 reported that published values of the gravitational acceleration range from 3.60 to 3.90 m/s^2 in 1968. Reference 19 gave the value as 3.71 m/s^2 in 1972, and 3.718 m/s^2 was used in constructing the models of the Martian atmosphere that were adopted in the 1974 revision of NASA 8010.

The most precise estimates of the product GM (often denoted by the symbol μ) have been determined from Mariner data. Two methods of reducing Mariner 6 data yielded the values 42828.22 ± 1.83 and 42828.48 ± 1.38 km^3/s^2, and an upgraded estimate from Mariner 4 data gave 42828.32 ± 0.13 km^3/s^2.

Since Mars is nonspherical and the gravity field varies over the surface, attempts were first made to approximate its variation by assuming Mars to be an oblate spheroid. A development of its gravitational potential U in a spherical harmonic series in terms of the latitude θ and radial distance r from the planet center was expressed as

$$U(r,\theta) = \frac{GM}{r}\left[1 - J_2\left(\frac{R_E}{r}\right)^2 P_{20}\right]$$

by terminating the series after the first two terms. The radial gravitational acceleration without centrifugal force subtracted is then given as

$$g = -\frac{\partial U}{\partial r} = \frac{GM}{r^2}\left[1 - 3J_2\left(\frac{R_E}{r}\right)^2 P_{20}\right]$$

where

$$P_{20} = \frac{1}{2}(3\sin^2\theta - 1)$$

A preliminary reduction of Mariner 9 data gave $J_2 = 0.001965 \pm 0.000006$, $GM = 42828.5 \pm 0.4$ km^3/s^2, and the equatorial radius $R_E = 3394 \pm 2$ km (ref. 105). The constant J_2 is a measure of the flattening f whose value is 0.00524 ± 0.00003.

Mariner 9 data indicated the gravity field to be an order of magnitude rougher than expected and to vary with azimuth and latitude. As a result, a more general potential function U has been adopted (refs. 103, 104, and 105).* The potential function and values of the parameters determined after additional analyses of Mariner 9 data are given in section 3.3. This more general gravitational function does not model completely such anomalies as noted in the Tharsis region which are many times larger than any found on Earth.

*Also, W. L. Sjogren et al., "Mars Gravity Field Based on a Short-Arc Technique," J. Geophys. Res., vol. 80, no. 20, 1975, pp. 2899-2908.

2.3.7 Magnetic Field

The results of Mariner 4, 6, and 7 magnetometer measurements indicate the field strength to be less than 0.001 of the Earth's magnetic field. From this, it is inferred that the magnetic moment of Mars is less than 0.001 that of the Earth and that the equatorial surface magnetic field of Mars is less than 200 γ (ref. 63). The Russian space probes Mars 2 and 3 have established the existence of a detached low shock wave in the solar wind as it flows past Mars. N. F. Ness and S. J. Bauer suggest that the obstacle deflecting the solar wind is an intrinsic planetary magnetic field in GSFC X-690-74-69, Goddard Space Flight Center, Greenbelt, Md., February 1974.

2.3.8 Morphologic Subdivisions

Morphologic subdivisions deduced from Mariner 6 and 7 photographic data included crater terrain (ref. 106) and uncratered terrain (ref. 107). Cratered terrain contains small bowl-shaped and large flat-bottomed craters. Uncratered terrain has regions that have an irregular jumble of topographic forms and regions that contain no resolvable topographic features.

The morphologic characteristics deduced from Mariner 9's extensive photographic coverage were subdivided into four classes: (1) primitive, cratered terrain; (2) sparsely-cratered, volcanic-aeolian plains; (3) circular, radially-symmetric volcanic constructs, such as shield volcanoes, domes, and craters; and (4) tectonic-erosional units such as chaotic material and channel deposits (ref. 108). According to Masursky (ref. 109), the primitive cratered terrain covers about one-half of the surface. Mariner 4, 6, 7, and 9 photographs indicate a range of crater types similar to those found on the Earth and Moon according to Hartmann (ref. 110). All three bodies contain the four types of crater morphology: (1) bowl-shaped, (2) central peaks, (3) interior rings of peaks, and (4) large basins. Hartmann finds that the relative number of craters of different sizes found in sparsely- and heavily-cratered regions are similar for Mars and the Moon.

Crater frequency distributions are expressed mathematically in reference 61 as $N = kD^{-n}$, where N is the cumulative number of craters per square meter having diameters larger than D, and n and k are constants. Frequency distributions corresponding to this equation have been adapted for this monograph and are presented in section 3.6.2 for an average Mars.

2.3.9 Topography

2.3.9.1 Elevation

Radar echoes received from Mars during each opposition since 1963 have been used to estimate elevation variations in the equatorial regions. More recently surface pressures obtained by occultation experiments on Mariner spacecraft have been used to derive estimates of surface elevations.

Mariner 9 improved upon earlier Mariner results because it was placed in orbit around Mars and provided occultation measurements at points around the planet (refs. 111, 112, and 113).

The variation of pressures with surface location shown by Mariner 9 and spectrographic results correlate with the topography of Mars.* Recent topographic estimates that have been derived from occultation, radar, spectral, and optical measurements show a range of elevations from 4 km below the mean surface in Hellas depression to an altitude of 28 km on Olympus Mons.**

The surface pressure data obtained by the Mariner 9 occultation experiment (ref. 114) and the gravity data*** suggest that the physical shape of Mars is not much more oblate than its gravitational equipotential surface. The latest compilation of all data** indicates that the shape is triaxial with equatorial radii of 3399.1 km for 110° West longitude and 3394.1 km for 20° West longitude and with a polar radius of 3376.7 km. Earlier results based on some of the same data give similar radii (refs. 39, 115, and 116).

2.3.9.2 Surface Topography

Two related descriptions of the surface topography are commonly used, and each has its own application. For studies of landing dynamics or vehicle hill-climbing, slope distributions are required. To determine the dynamic response of a vehicle traversing the terrain, power spectral density (PSD) is needed to describe surface roughness.

a. Slope Distribution

As an illustration of slope distribution consider two points on the Martian surface a distance L apart with a difference Δh in elevation between the two points. The two distances define the slope α between the points. If measurements of the slope are made between many pairs of points along a traverse on the surface, a distribution of slopes is obtained (ref. 117). This distribution can be described statistically in terms of a probability density function $P(\alpha)$ or a cumulative distribution function $F(\alpha)$. From such distributions of slopes, an "average" or mean value, a median value, and other statistical parameters can be obtained.

Although slope distributions are not necessarily Gaussian, measurements of slopes can be described approximately in terms of a mathematical model corresponding to a so-called Gaussian or "normal" distribution. For example, the probability density function

$$p(\alpha) = \frac{1}{\sigma\sqrt{2\pi}} \exp\left(-\frac{\alpha^2}{2\sigma^2}\right) \quad (-\infty < \alpha < \infty)$$

*Besides variation with topography, seasonal variation of surface pressure by 10 to 20 percent is indicated in recent study by P. M. Woicestyn, "Global Seasonal Fluctuations on Mars," Icarus 22, July 1974.

**E. J. Christensen, "Martian Topography Derived from Occultation, Radar, Spectral and Optical Measurements," Journal of Geophysical Research, vol. 80, no. 20, 1975, pp. 2909-2913.

***W. L. Sjogren et al., "Mars Gravity Field Based on a Short-Arc Technique," J. Geophys. Res., 80, 20, 1975, pp. 2899-2908.

describes a normal distribution with an (algebraic) mean of zero and a standard deviation σ. Because the (algebraic) mean from slope measurements is often very nearly zero, it is customary to ignore the algebraic sign of the slope and work with its magnitude alone. Thus, the "mean slope" α is defined with absolute values as

$$\alpha = \int_{-\infty}^{\infty} |\alpha| \, p(\alpha) d\alpha$$

For slope distributions which are normal (Gaussian), the mean (absolute) slope is related to the standard deviation by

$$\alpha = \sqrt{\frac{2}{\pi}} \sigma$$

This theoretical relationship is in close agreement with an empirical relation

$$\alpha = 0.79 \, \sigma$$

given by Rowan, McCauley and Holm (ref. 118) for the Moon which is based upon extensive Earth-based measurements at slope lengths of 0.75 km and larger.

The mean slope $\bar{\alpha}$ depends on the horizontal distance L between the points having the elevation difference Δh. Measurements of $\bar{\alpha}$ on the surface of the Earth, Moon, and Mars indicate roughly a linear relation between log α and log L. Thus, the mathematical form relating $\bar{\alpha}$ and L is approximated by an equation of the form $\alpha = bL^{-n}$. The approximate values of b and n as estimated from Figure III-C-8 in reference 61 are b = 1, 3, and 14 degrees and n = 0.10, 0.18, and 0.28, corresponding to smooth, nominal, and rough Martian surfaces, respectively. Slope data deduced from radar data indicate the mean Martian slope is a little lower than the Smooth Lunar Mare at 1 to 2 m and 10 to 100 km base lengths.

b. Surface Roughness

For vehicle dynamic studies the local variations in the elevation h along a given traverse is of more interest than the slope α. In this case, the terrain roughness profile is conveniently described in terms of power spectral density. Jaeger and Schuring (ref. 119) present data for the Ranger 7 site (Mare Cognitum) and a procedure that utilizes the data to determine the dynamic response of a vehicle moving over the surface. The use of spectrum analysis procedures for describing lunar surface roughness is described by Rozema (ref. 120).

Data obtained from Mars to date have not been of sufficient resolution nor for a long enough traverse to justify power spectral density computations of the type made for the Moon by R. Pike and his coworkers at USGS. As a result, the power spectral density models presented in section 3.5.4 are derived from lunar and terrestrial data.

2.3.10 Crater and Block Frequencies

The first Martian crater frequency data were provided by Mariner spacecraft. Reference 33 gives comparisons of Martian crater frequency distributions with distributions for the lunar Maria and Uplands. The Martian crater diameters range from about 7 to 200 km. Reference 106 compares crater frequencies obtained from Mariner 9 data for the Deucalionis Regio region with craters in the lunar Maria and Uplands. Crater frequencies are shown for crater dimensions ranging from about 500 m to 70 km. The data indicate overall crater frequency distributions are similar, but the Martian bowl-shaped craters occur less frequently than the same size lunar craters.

The resolution of Mariner photographs is not sufficient to provide block frequency data so the models adopted here were developed from lunar block frequencies.

2.3.11 Soil Characteristics

The interaction of the Martian surface with incident solar radiation allows remote deduction of soil properties. Remote sensing of the planet by infrared emittance spectroscopy can provide information on the mineral composition of the surface material and its particle sizes and concentrations (ref. 121).

The most serious problem in acquiring Mars spectral data is from atmospheric effects on Mars (and on Earth during Earth-based observations) which limit the available wavelength range and attenuate and distort spectral information. Another difficulty is that the composition and grain size of the surface material may not be homogeneous over an area as large as the spatial resolution of the instruments used in remote sensing. Also, the available energy for spectroscopic experiments is limited by the solar constant, the relative position of Earth and Mars, and Martian interaction with solar energy (ref. 122).

Spectral observational data available as of 1969 for the visible (0.4 to 0.7 μm), the near-infrared (0.7 to 2.5 μm) and the mid-infrared (2.5 to 500 μm) ranges were reviewed by Salisbury and Hunt in reference 122.

2.3.11.1 Composition

Some of the first observations of the Martian surface consisted of polarization measurements made at the Pic du Midi Observatory. Comparisons of polarization measurements of Mars and terrestrial materials in the visible wavelength range led Dollfus (ref. 74) to conclude the Martian surface was primarily limonite, a hydrated iron oxide. Limonite is a term used to describe minerals which contain mixtures in various proportions of hematite, geothite and unspecified impurities (ref. 123).

Sagan (ref. 18), Tull (ref. 124), and Egan (ref. 125) have supported limonite as a primary material at the surface. Others have rejected the limonite hypothesis, including Younkin (ref. 123) and Houck et al. (ref. 46).

Caldwell analyzed ultraviolet data in the range 0.2 to 0.36 μm obtained from the Orbiting Astronomical Observatory (ref. 126). He found that when the reflectivity due to CO_2 is taken into consideration the remaining reflectivity from the surface disagrees with published ultraviolet reflectivities of limonite and carbon suboxides. Earlier, Sinton (ref. 127) had rejected limonite but concluded that iron oxides, although not a principal constituent, may be present as an impurity in sufficient amounts to color the surface red.

Hanel et al. (ref. 44) discuss characteristics of the Mariner 9 IRIS spectral features (Christiansen frequency shift) and those measured by Conel on terrestrial silicates. From these comparisons it was concluded that the composition of dust suspended in the Martian atmosphere was 60 ± 10 percent SiO_2, and that this percentage was also believed to be representative of the Martian crust material.*

Hunt (ref. 128) found that characteristics of the surface emission spectrum are sensitive to changes in particle size, packing density, pressure, and background temperature. It was noted that clay montmorillonite exhibits spectroscopic properties that closely match Martian data. Not only does montmorillonite display two major bands in the appropriate positions in the mid-infrared and lack any intense subsidiary, but it also displays bands near 0.95, 1.4, and 1.9 μm in the near-infrared.

Radar data at 3.8 and 70 cm wavelengths led Pettengill (ref. 25) to conclude the surface material is fairly homogeneous on a scale from 4 to 70 cm.

2.3.11.2 Particle Size

Morrison et al. (ref. 92) used 8 to 13 μm radiometry measurements by Sinton and Strong to obtain the distribution of temperature over the Martian surface. On the basis of thermal variation of the Martian surface, they estimated the mean particle sizes to be 25 to 250 μm for the bright areas and 100 to 300 μm for the dark areas. These values are in agreement with estimates made by Pollack (ref. 65) but are larger than those by Leovy (ref. 93). Leovy concluded from a study of diurnal temperature variations that the Martian surface had a layer of very fine powder whose characteristic size was not more than a few microns. Particle diameters were estimated from 2.0 to 4.0 μm reflectivity data by Houck et al. (ref. 46) to range from 20 to 300 μm with a mean value of 200 μm.

In reference 40 qualitative comparisons were made of the computed spectra with spectra measured by the infrared spectroscopy experiment on Mariner 9. The comparison suggested the radii of particles picked up from the surface to form the dust cloud were on the order of a few microns. This particle size is also in agreement with the size estimated by Koval (ref. 62).

2.3.11.3 Density

The bulk density of the lunar soil is in the range 1 to 2 g/cm^3. Density of the particle grains at the Apollo 11 and 12 sites was 3.1 g/cm^3 (ref. 97). This density range for the bulk

*R. L. Huguenin, "The Formation of Goethite and Hydrated Clay Materials on Mars," J. Geophys. Res., 79, Sept. 1975, pp. 3895-3905, shares this belief from his laboratory studies on the kinetics and mechanism of the photostimulated oxidation of magnetite and preliminary laboratory data on the weathering of silicates.

density encompasses the value of 1.2 g/cm^3 used by Balsamo and Salisbury (ref. 101) in their studies of the frost formation on Mars. Mars density values deduced by Troitskii ranged from 0.7 to 1.3 g/cm^3 (ref. 100). Estimated densities for the Martian soil models presented in reference 62 ranged up to 1.8 g/cm^3.

2.3.11.4 Porosity

Representative values of the porosity of the lunar soil is about 45 ± 10 percent (ref. 97). This range includes the porosity value of 50 percent used in the analyses of polarization data made by Egan (ref. 125).

2.3.11.5 Cohesion and Internal Friction Angle

Estimates of the cohesion and interval friction angle of the Martian soil are not deduced from remote sensing of Mars. The most probable range is that found for the lunar soil. Values of cohesion for the lunar soil lie in the range 0.003 to 0.21 N/cm^2 as determined from soil at the Apollo 11, 12, and 14 sites (ref. 97). The same data indicate internal friction angles to be 35 to 45 degrees.

2.3.11.6 Bearing Capacity and Penetration Resistance Gradient

The bearing capacity and penetration resistance gradient are strong functions of the soil density. They also depend on cohesion, internal friction angle, and bearing area. A typical value of bearing capacity quoted for the lunar soil is 3.5 N/cm^2 (ref. 97). The penetration resistance gradient measured by the Apollo 15 sample penetrometer records were 4.0 N/cm^2/cm in virgin soil and 5.2 N/cm^2/cm in compacted soil in the track of the Lunar Roving Vehicle (ref. 97). These values should be representative average values for the Martian soil.

2.3.12 Electrical Properties

2.3.12.1 Dielectric Constant

The dielectric constant of a material is a measure of the capability of the material to store and dissipate electric energy. It is conveniently expressed as a single complex quantity $\epsilon = \epsilon' + i\epsilon''$, where ϵ' and ϵ'' are measures of the energy storing and dissipative properties, respectively. Sometimes the complex coefficient is written as $\epsilon = \epsilon' (1 + i \tan \delta)$ where $\tan \delta = \epsilon''/\epsilon'$ is called the loss tangent. In general, ϵ' and ϵ'' depend on temperature, frequency, packing density, particle size, and possibly other parameters.

Extensive investigations of the electrical properties of terrestrial rocks in solid and powder forms were conducted by Campbell and Ulrichs (ref. 129) to assist in the interpretation of radar data. Measurements were made at 0.88 cm and 67 cm to correspond to the wavelengths spanned by current radar and radiometric observations of Mars. The data indicated a range of dielectric constants from about 2.5 for pumice to about 9.5 for some basalts. Data for powders indicated the variation of ϵ' and tan δ with density agreed quite

well with the Rayleigh mixing formula for many of the materials. Values for the powder were substantially lower than for solid rocks. For example, the value of ϵ' for solid olivine basalt was 8.1 at 0.67 cm wavelength; the corresponding value for a powder of the same material was about 2.0 at a density of 1 g/cm^3.

The dielectric properties of a large number of other terrestrial materials are summarized in references 130 and 131. At low frequencies the dielectric constant for water is listed as 78.54 at 298 K and for carbon dioxide as 1.60 at 293 K in reference 130.

Dielectric properties measured on lunar regolith and rock samples returned to Earth by the Apollo program are summarized in reference 97. Typical values for some lunar rocks were 8.0 ± 0.8 in the wavelength range 30 m to 3 × 10^5 m. Measurements made on lunar rock powders by Gold et al.* indicated values of ϵ' ranging from 1.7 to 2.5 as the powder density increased from 0.9 to 1.6 g/cm^3.

The first estimates of dielectric properties of the Martian surface material were based on values measured for terrestrial materials. Fine-grained soil material was used in the estimates because the indicated Martian dust storms presupposed that type soil. In reference 1 the dielectric constant was estimated to be 5.2 ± 3.0 from various combinations of tuff, andesite basalt, and carbon dioxide with a range of packing densities.

Pettengill deduced the dielectric constant from 3.8 cm radar data obtained at the Haystack Observatory during the 1967, 1969, and 1971 oppositions. From 1969 data (ref. 25) he indicated 3.5 to be a typical dielectric constant. His 1971 data indicate that at −14° latitude the dielectric constant increases steadily from 1.7 at 70°W to about 5.0 at 110°W (ref. 27). These results appeared to show a definite correlation between dielectric constant and surface roughness. If each of the N data measurements are weighted equally, the average dielectric constants ϵ for each of the three years are N = 114 and ϵ = 2.07 for 1967, N = 264 and ϵ = 2.77 for 1969, and N = 1674 and ϵ = 3.65 for 1971. It is generally agreed that reflectivity and surface roughness vary by factors of 5:1 from point to point on the surface. Hence, differences in the dielectric constants deduced from data obtained along the radar ground track during the three oppositions may simply reflect regional variations. Some of the differences in dielectric constant estimates also may result from differences in transmitter power and analysis procedures used in reducing the reflectivity data obtained during the three oppositions. Dielectric constants deduced by other investigators or used by them in their analyses were 3.0 (ref. 125), 2.6 ± 0.8 (refs. 83 and 100), 2.80 (ref. 28), and 5 (ref. 82).

2.3.12.2 Loss Tangent

Loss tangents for various terrestrial rocks listed in reference 129 range from a low value of about 0.004 to a high of about 0.09 at 0.86 cm and 67 cm wavelengths. Reference 129 gives tan δ = 0.017 for solid olivine basalt; the value for the powdered form at 1 g/cm^3 density is 0.005.

*T. Gold, M. J. Campbell, and B. T. O'Leary, "Optical and High Frequency Electrical Properties of the Lunar Sample," Science, vol. 167, Jan. 30, 1970, pp. 707-709.

The values of the loss tangent deduced from Martian data by Morrison et al. (ref. 66) for the surface material was 0.03 and by Ulich et al. (ref. 89) from 0.0084 to 0.0492. The value adopted by Efanov ranged from 0.0032 to 0.0156 (ref. 83). The value deduced by Troitskii from his basic surface model ranged from 0.005 to 0.017 (ref. 100). These values are approximately in the range recommended for the lunar surface materials in reference 97 of $0.005 \leq \tan \delta \leq 0.13$ for lunar soils and $0.01 \leq \tan \delta \leq 0.14$ for lunar rocks.

2.3.13 Photometric Properties

Photometric properties of a planet are often described in terms of integrated properties of the total planetary emission or detailed properties of local emissions from point to point over the planetary disk (refs. 35 and 132). Measurements of the local photometric properties of Mars from Earth-based observations are severely limited because of the small apparent disk. Also a limitation for the determination of the integrated phase function is that needed brightness measurements are only possible over incidence angles smaller than 48 degrees (ref. 132). Data obtained in the vicinity of Mars by Mariner spacecraft have provided new information for the refinement and extension of detailed and integrated photometric properties of Mars.

2.3.13.1 Photometric Function

A photometric function was developed by J. J. Lambiotte by combining Martian data measured at small angles with photometric measurements of soils believed to be optically similar to the Martian surface (ref. 61). Subsequently Meador and Weaver (ref. 138) developed a photometric function on a different theoretical basis and that showed improved correlations with the reflective properties of the surfaces measured in the laboratory. Dimensionless parameters in the improved model (denoted by a_0, a_1, and a_2 and depending on such surface properties as particle size, porosity, and particle albedo) were estimated by Weaver, Wood, and Meador (ref. 139) with Martian photometric data obtained by Mariner 9 (ref. 140). These Martian data were obtained at an effective wavelength of 0.56 μm. At the present time Martian photometric data at other wavelengths are not available for extending the photometric functions outside $\lambda = 0.56 \pm 0.14$ μm.

2.3.13.2 Albedo

Albedo (also known as Bond albedo) is an integrated photometric property used as a measure of the reflectivity of a planet. The measure was originally proposed by Bond and adopted in 1916 (ref. 134). It is defined as the fraction of solar radiation falling on a planet that is reflected in all directions.

Reference 31 indicates the average Bond albedo for the whole of Mars increases from 0.05 or less in the ultraviolet and blue regions of the spectrum to more than 0.3 in the red and infrared. The average value for the visible spectrum (0.35 to 0.7 μm) is about 0.17; the value over the entire spectrum is 0.295. Bright areas have a somewhat higher average albedo, whereas darker areas have a smaller average albedo (ref. 135).

Bond albedo values given by Evans range from 0.04 to 0.08 in the ultraviolet range (0.25 to 0.35 μm, ref. 136). Evans finds the albedo in the ultraviolet region increases toward shorter wavelengths according to a Rayleigh law. This behavior is also shown in data obtained from the Orbiting Astronomical Observatory presented by Owen and Sagan (ref. 38). They find the variation in reflectivity at short wavelengths is consistant with Rayleigh scattering by a CO_2 atmosphere having a 5.5 mb surface pressure. Caldwell (ref. 126) found that when the reflectivity contributed by the known amount of CO_2 in the atmosphere was taken into account the surface reflected 50 to 65 percent of the total albedo.

In 1970 McCord et al (ref. 137) found agreement and disagreement among available measurements for various localities. Comparisons of Arabia and Syrtis Major albedo show that Arabia is about 3 times brighter over most of the wavelength range from 1 to 2.5 μm.

The variation of normal albedo with wavelength was determined from Earth observations (ref. 61) for the Desert and Mare regions. These results are adopted and presented in section 3.10.2.

3. CRITERIA

The Martian surface models and related physical, chemical, and mechanical properties presented here should be used for mission analyses and for design of landing and exploration vehicles. For the Martian atmosphere, NASA SP-8010 (Revision of 1974) provides engineering models that take into account variations in Martian time of day, season, location, and solar activity.

3.1 Nominal Geophysical Parameters

Nominal, or average, properties of Martian geophysical parameters are listed in table 1.

3.2 Atmospheric Properties

3.2.1 Composition

Major constituents of the atmosphere are carbon dioxide, nitrogen, and argon or some other inert gas. Such inert gas or gases may account for about one third of the total gas abundance. Nitrogen accounts for one percent, and CO_2 accounts for the balance except for minor constituents. They make up 1 to 2 percent and consist of water vapor, dust, CO, O_2, and O_3.

3.2.2 Surface Pressure

Mariner 9 data indicated the average surface pressure to be 4.8 mb in the equatorial zone. Surface pressures ranged from 1.5 mb at the top of Arsia Mons to about 8 mb in the Hellas depression. Figure 1 relates local atmospheric pressure to surface elevation referenced to the areoid containing the mean equatorial radius.

Table 1
Nominal Geophysical Parameters

Parameter	Nominal Value	Reference
Equatorial radius (km)	3397.2 ± 1	105
Polar radius (km)	3375.5 ± 1	105
Flattening (dimensionless)		
Dynamical	0.0054 ± 0.00002	104
Optical	0.0057	105
Mass (g)	6.418×10^{26}	104
Density (g/cm^3)	3.933	*
Gravitational Constant, $\mu = GM$ (km^3/s^2)	42828.32	105
Gravitational Acceleration (m/s^2)	3.71	*
Escape Velocity (km/s)	5.024	3
Nominal Surface Pressure (mb)	4.8	61
Surface Temperature (K)		
Equatorial		
Minimum	172	91
Maximum	289	91
Polar		
Minimum	150	91
Maximum	220	91
Sidereal Period of Revolution (days)	686.9804	3
Sidereal Period of Rotation (hr;min;s)	24;37;22.6689	3
Distances from Sun (km)		
Mean (semi-major axis)	227,800,000	3
Perihelion	206,500,000	3
Aphelion	249,100,000	3
Distance from Earth (km)		
Minimum	55,810,000	3
Maximum	398,900,000	3
Mean Opposition	78,350,000	3

*Calculated

3.2.3 Viscosity and Specific Heat Ratio

The viscosity of the atmosphere is estimated to lie within the range 0.6×10^{-5} to 2.4×10^{-5} kg/m s. The specific heat ratio is within the range of 1.3 to 1.4.

3.2.4 Surface Winds

The maximum steady wind velocity above the boundary layer is 70 m/s. Gusts within the boundary layer can be assumed to have a 3σ value equal to 35 m/s. The variation of the steady wind velocity within the boundary layer is shown in figure 2.

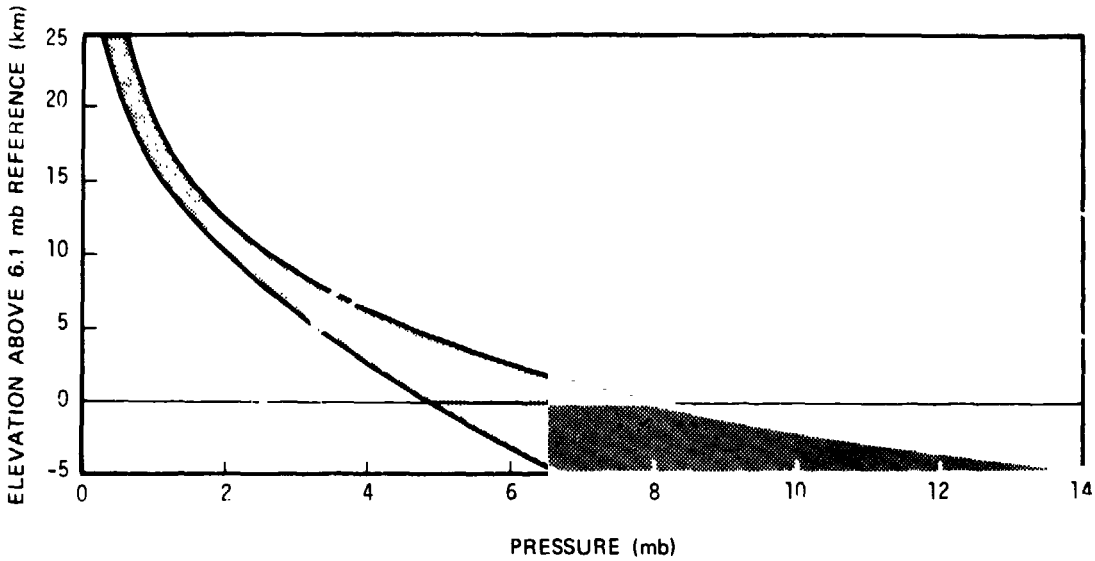

Figure 1. – Range of Surface Pressure Above Nominal 6.1 mb Reference Geoid (Derived from ref. 61).

3.2.5 Entrained Dust

Figure 3 presents estimates of the minimum wind speed one meter above the surface required to initiate motion of the surface particles. The major portion of the moving particles will be by saltation. Although the top of the saltating layer may extend many meters above the surface, the bulk of the grains move within the first meter above the surface. The estimated flux of moving particles up to two meters above the surface is shown in figure 4. The maximum total flux per unit width along the surface is 1 g/cm s. The saltating particles can be considered to range in size up to 1000 μm diameter and to have the same size distribution as the dune sand shown in section 3.7.5. The maximum velocity of the saltating grains shown in figure 4 over the first 2 meters can be assumed to be 25 m/s.

During a typical storm the dust entrained in the atmosphere may extend several kilometers above the surface. Estimates of the amount of dust that settles on a horizontal surface after the dust storm range from 10 to 1000 g/m^2. An atmospheric model for a typical dust storm is given in NASA SP-8010 (Revision of 1974).

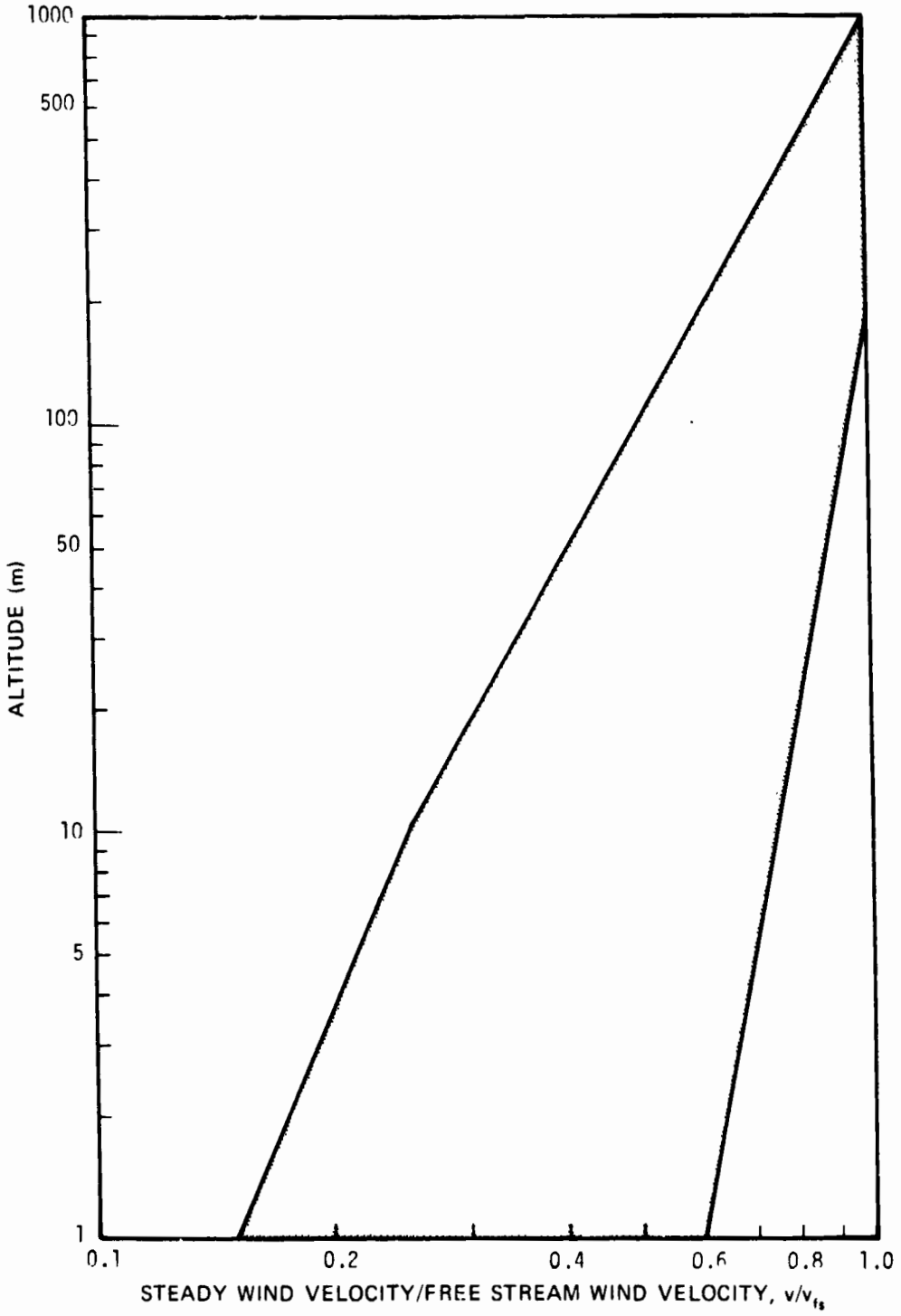

Figure 2. – Steady Wind Velocity Ratio Through the Boundary Layer (ref. 61).

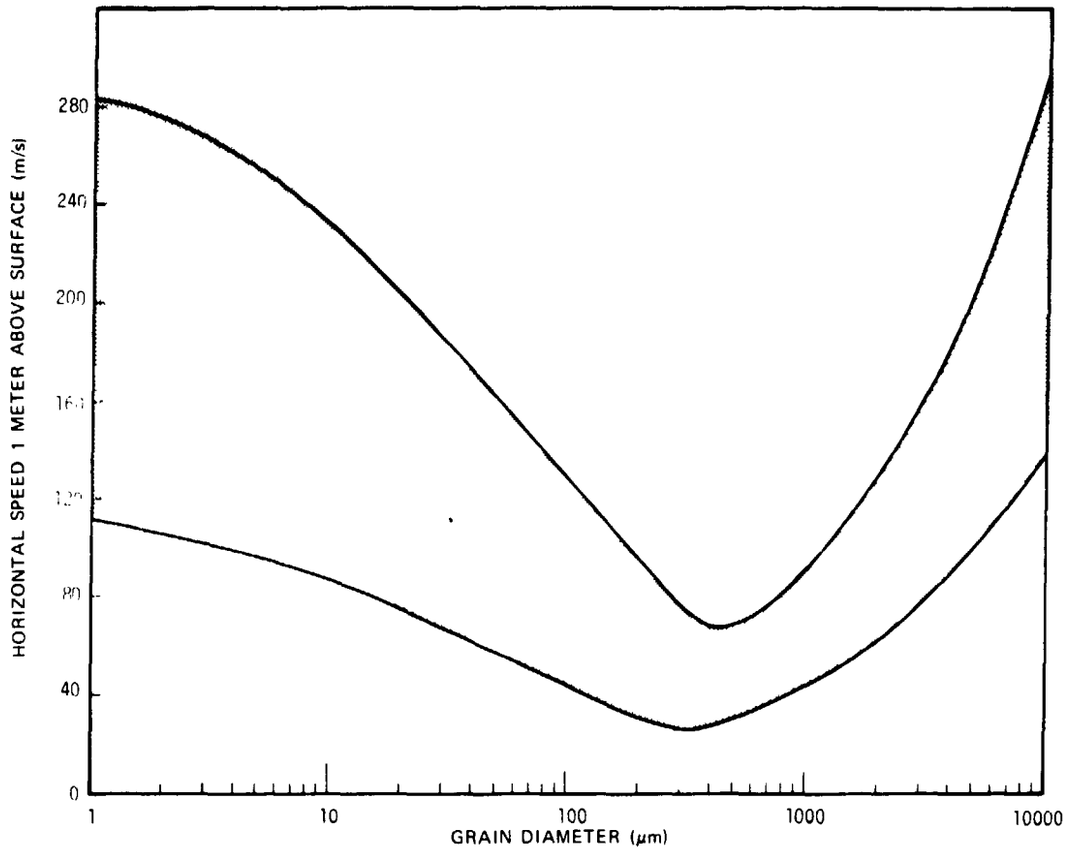

Figure 3. – Range of Minimum Wind Speed One Meter Above Surface to Initiate Particle Motion (ref. 61: Based on Bagnold Theory Using 3 Model Atmospheres for Roughness of 0.003 to 0.1 cm).

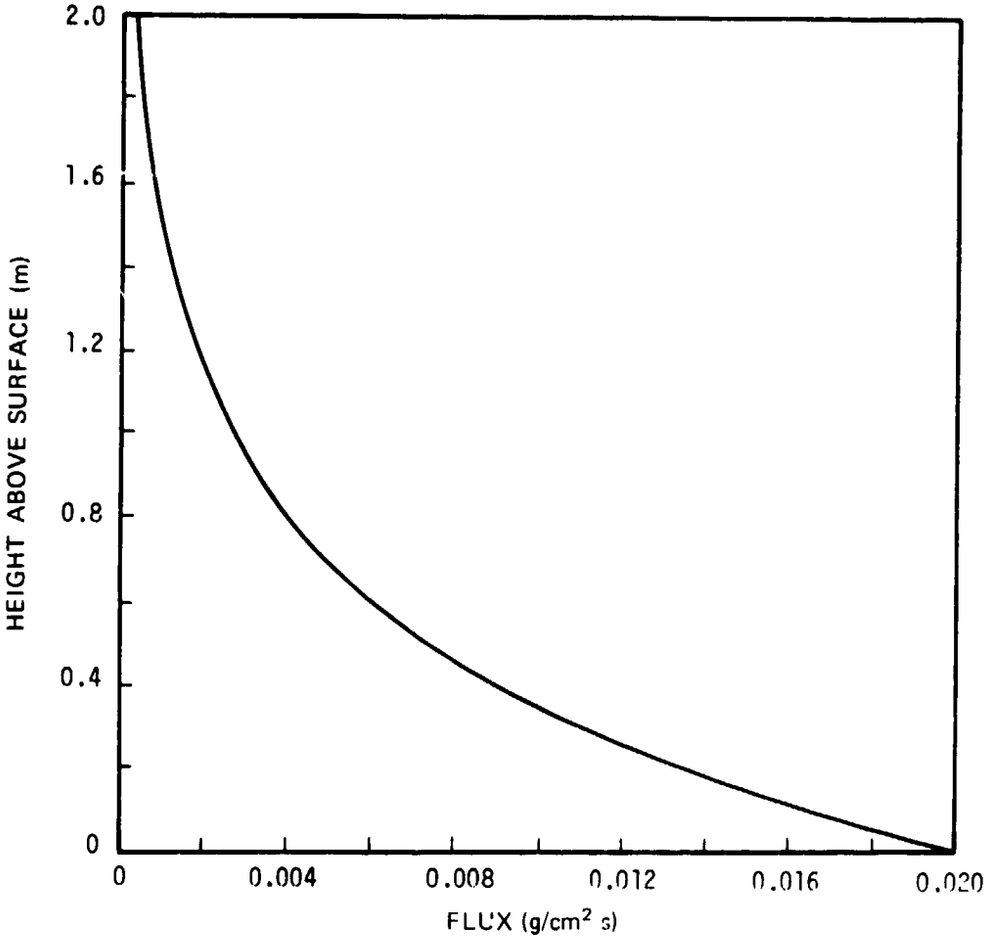

Figure 4. – Saltating Sand Flux (ref. 61).

3.3 Gravitational Field

The gravitational field potential U is expressed in terms of fourth degree spherical harmonic expansions (refs. 19 and 105)

$$U = -\frac{GM}{r}\left\{1 - \sum_{n=2}^{4} J_n \left(\frac{R}{r}\right)^n P_{no}(\sin\theta) + \sum_{n=2}^{4}\sum_{m=1}^{4} \left(\frac{R}{r}\right)^n P_{nm}(\sin\theta)\left[C_{nm}\cos m\lambda + S_{nm}\sin m\lambda\right]\right\}$$

where the coefficients J_n, S_{nm} and C_{nm} are listed in table 2, and where

r = radius vector to an arbitrary point
R = mean equatorial radius (corresponding to 3394 km for the coefficients in table 2)
GM = gravitational constant μ in table 1
P_{nm} = associated Legendre polynomials
θ = latitude
λ = longitude (degrees east)

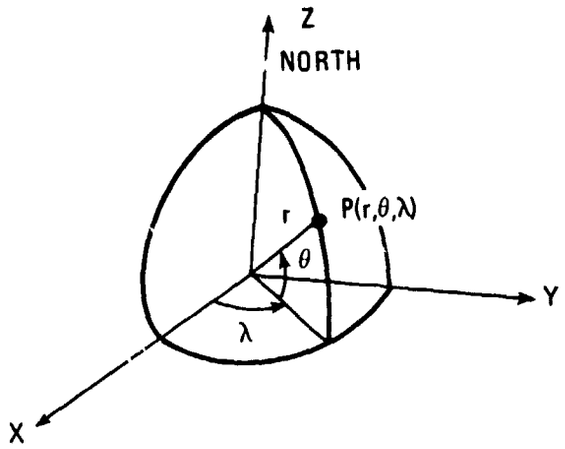

The gravitational acceleration g at an arbitrary point P(r, λ, θ) is obtained from the partial derivative of the gravitational potential function by the equation

$$g = -\frac{\partial U}{\partial r}$$

Table 2
Coefficients in Gravitational Potential Function

Coefficient*	Value (factor = 10^{-4})	Coefficient	Value (factor = 10^{-4})
J_2	19.65 ± 0.06		
J_3	0.36 ± 0.20		
J_4	− 0.29 ± 0.40		
C_{22}	−0.548 ± 0.010	S_{22}	0.31 ± 0.02
C_{31}	0.048 ± 0.040	S_{31}	0.26 ± 0.05
C_{32}	−0.055 ± 0.020	S_{32}	0.026 ± 0.020
C_{33}	0.048 ± 0.003	S_{33}	0.035 ± 0.003
C_{41}	0.025 ± 0.060	S_{41}	0.019 ± 0.070
C_{42}	−0.0063 ± 0.0100	S_{42}	−0.024 ± 0.020
C_{43}	0.0037 ± 0.0030	S_{43}	0.00015 ± 0.00200
C_{44}	−0.00023 ± 0.00070	S_{44}	−0.0025 ± 0.0010

*The coefficients C_{21} and S_{21} are taken to be zero in the expansion (refs. 84 and 96).

3.4 Magnetic Field

From Mariner 4, 6, and 7 magnetometer measurements it is inferred that the equatorial surface magnetic field is less than 200γ.

3.5 Terrain Properties

3.5.1 Morphology

Four classes of units are recognized on Mars: (1) primitive cratered terrain, (2) sparsely cratered volcanic aeolian plains, (3) circular radially symmetric volcanic constructs such as shield volcanoes, domes, and craters, and (4) tectonic erosional units such as chaotic and channel deposits. A generalized geological map which delineates these units between the latitudes 65 S and 65 N is shown in figure 5.

3.5.2 Elevation

Recent topographic estimates that have been derived from occultation, radar, spectral, and optical measurements show a range of elevations from 4 km below the mean surface in Hellas depression to an altitude of 28 km on Olympus Mons as shown in figure 6.

Local elevation contours of selected regions having substantial relief and of geological interest are shown in figures 7a, b, c (USGS, upgraded versions of the photomaps in ref. 113). Figure 7a shows Olympus Mons, the largest of the Martian shield volcanoes. The structure is approximately 600 km across and is located at 18°N, 134°W. Figure 7b shows Pavonis Mons (Middle Spot). It is another shield volcano located at 1°N, 113°W and is about 400 km across. Figure 7c shows a portion of a 4800 km long canyon system called Valles Marineris at about 8°S and 84°W.

3.5.3 Mean Slope and Cumulative Frequency

The variation of mean Martian slope $\bar{\alpha}$ with base length L is shown in figure 8. The variation of slope α about the mean slope can be determined from the cumulative frequency function

$$N = e^{-\alpha/\bar{\alpha}}$$

where N represents the fraction of slopes steeper than angle α.

3.5.4 Power Spectral Density

Power spectral density models recommended for Mars are presented in figure 9 as derived from terrestrial and lunar data.

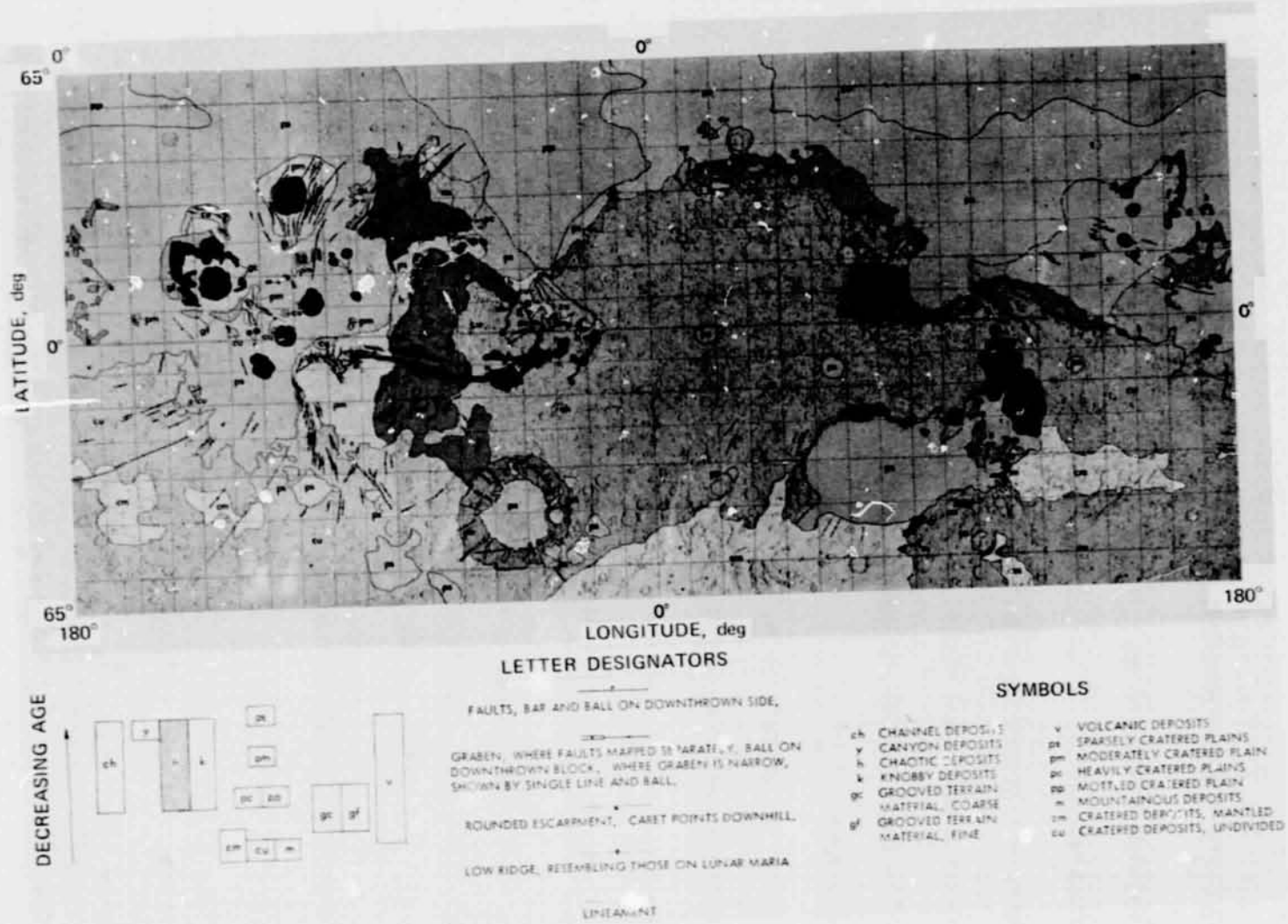

Figure 5. — Generalized Geologic Map Between 65°N and 65°S (ref. 108).

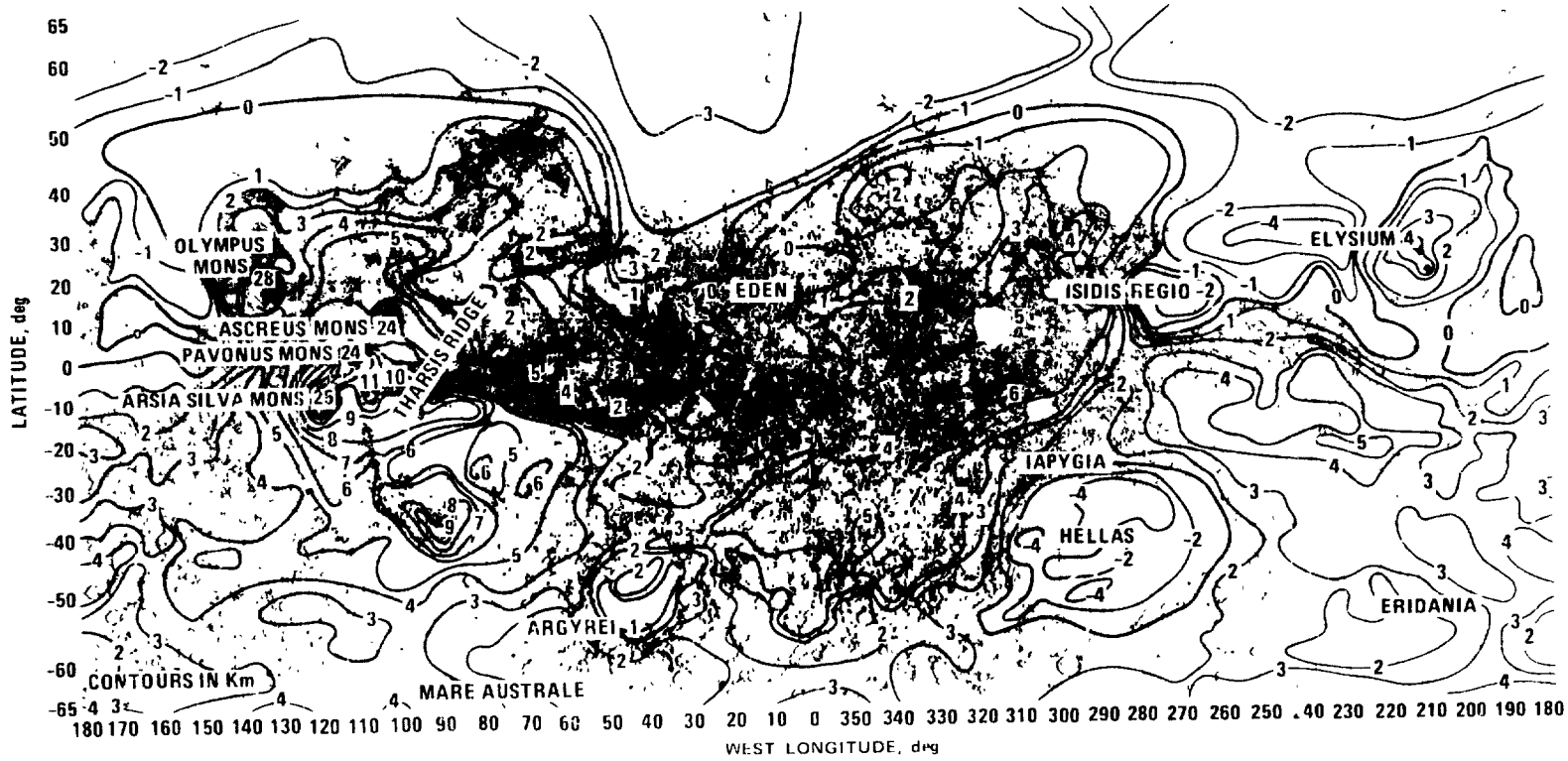

Figure 6. – Topographic Map of Mars (Altitudes in km) (ref. 142).

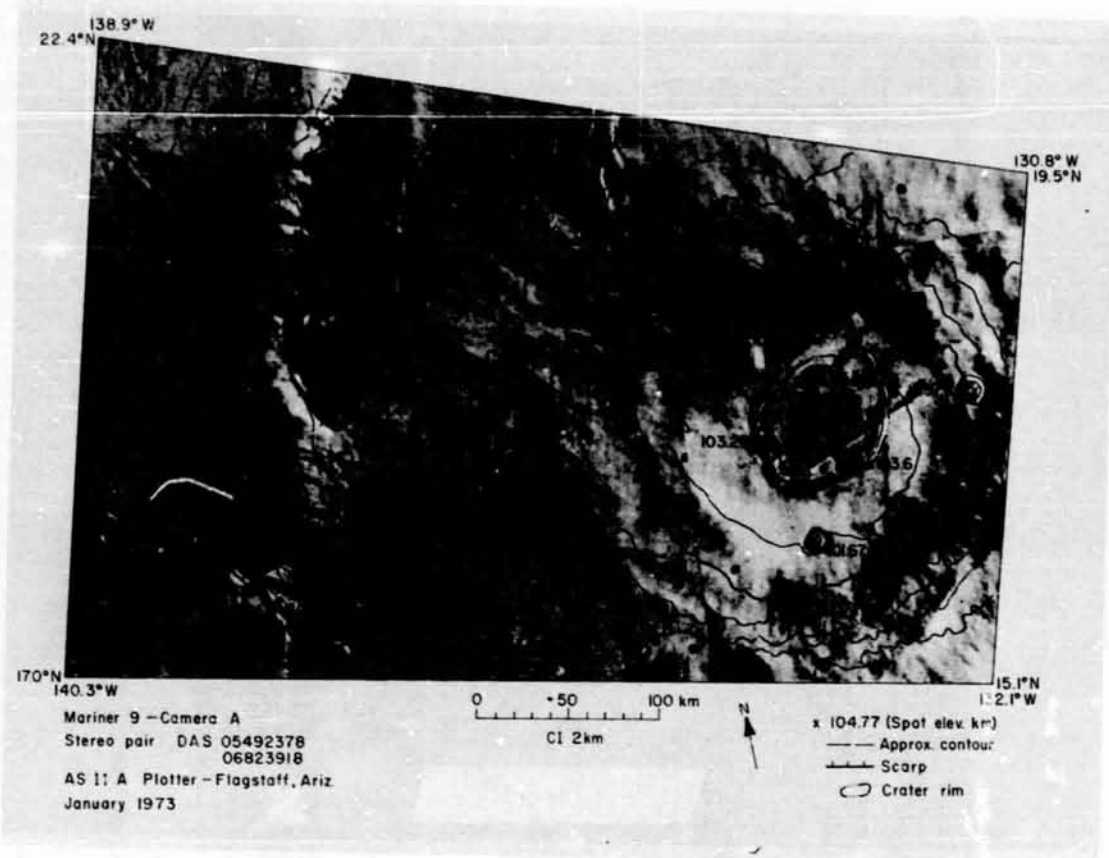

Figure 7a. – Relative Elevations at 2 km Intervals of Olympus Mons from Mariner 9 Camera (ref. USGS, Flagstaff, Ariz.).

3.6 Craters and Blocks

3.6.1 Morphology

The cratered regions of the Martian surface have been subdivided into the two regions called (1) heavily cratered provinces, and (2) sparsely cratered provinces. The maximum crater frequency model presented here corresponds roughly to the saturation crater frequency distribution, whereas the nominal and minimum curves correspond approximately to the crater distributions seen in heavily and sparsely cratered provinces. A range of crater forms starts at small diameters with small bowl-shaped craters, proceeds through craters having central peaks, extends to craters having interior rings on the crater floor, and ends with the largest crater basins in which all manifestations of central mountains have disappeared (refs. 108 and 110).

Current Martian photographs do not have sufficient resolution to provide block data. The models presented here are taken to be the same as those for the Moon. A standard Martian

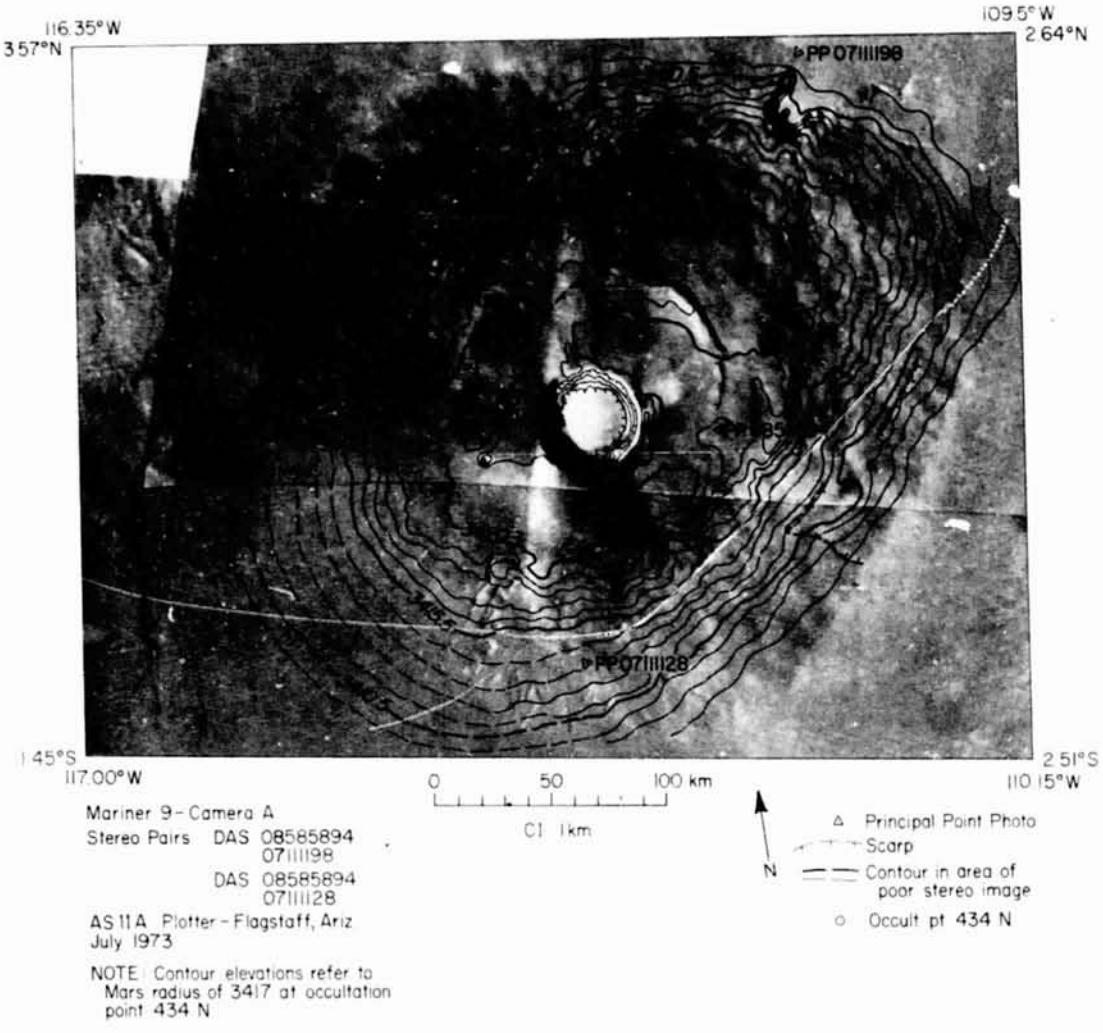

Figure 7b. – Relative Elevations at 1 km Intervals of Pavonis Mons from Mainer 9 Camera (ref. USGS, Flagstaff, Ariz.)

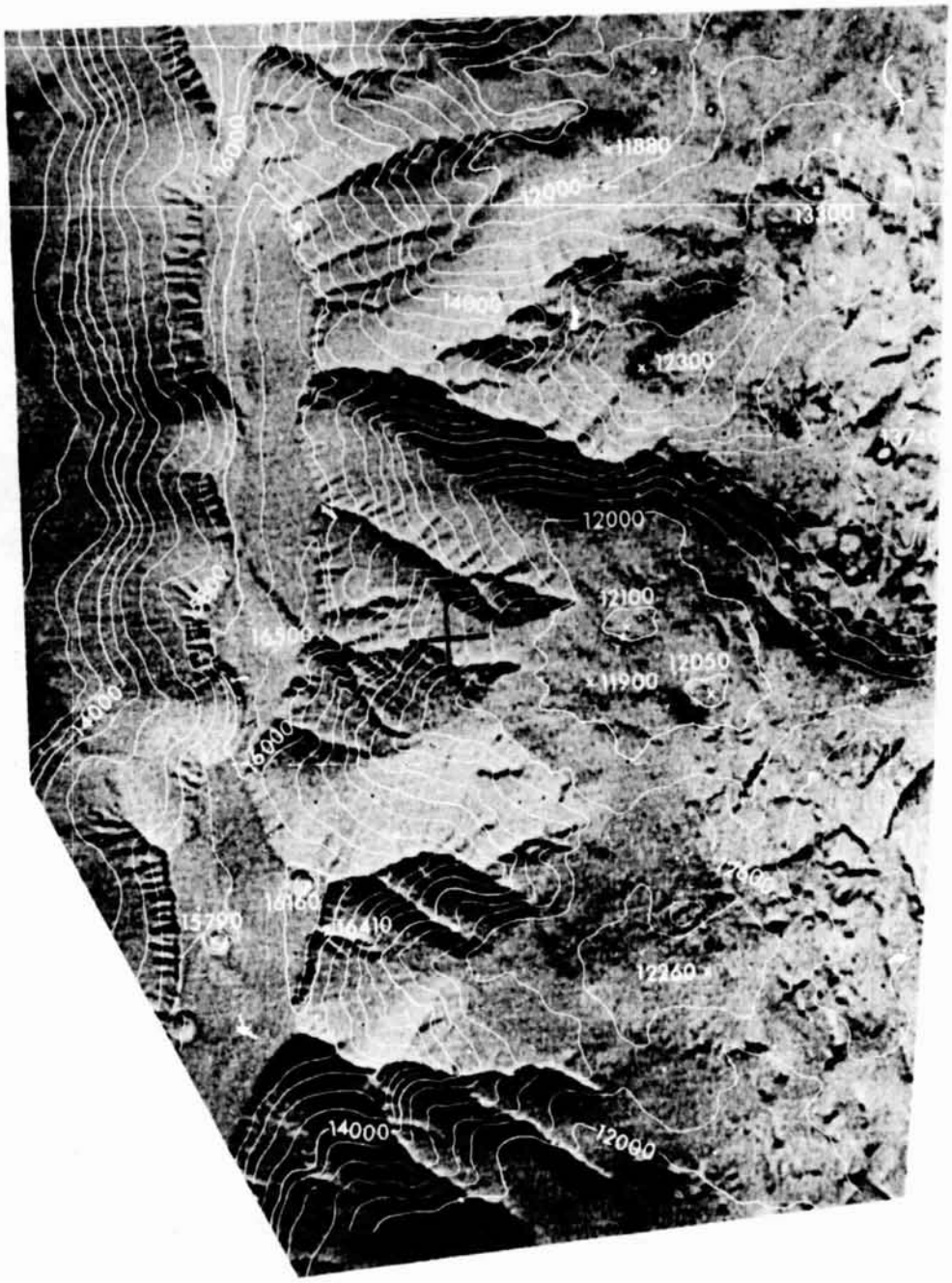

Figure 7c. – Relative Elevations at 400 m Intervals for Canyonlands at About 8°S and 84°W from Mariner 9 Camera (ref. USGS, Flagstaff, Ariz.).

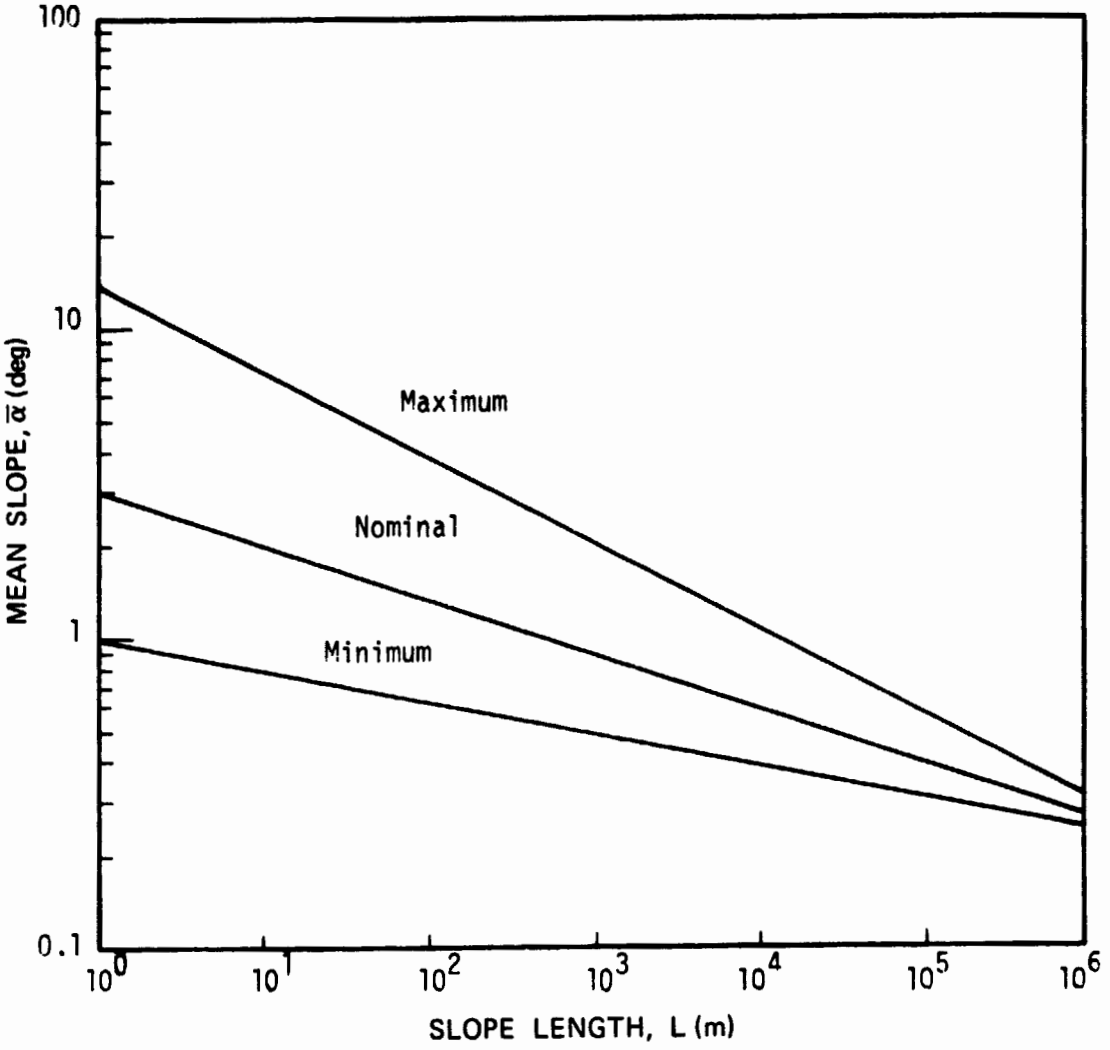

Figure 8. – Mean Surface Slope (ref. 61).

block can be considered as one having a ratio of its longest dimension to its shortest dimension in the range 1:1 to 5:1. Block surfaces may be rounded or rectangular, and they may be pitted, eroded, or vesiculated.

3.6.2 Frequency

Cumulative numbers of craters and blocks are shown in figures 10 and 11.

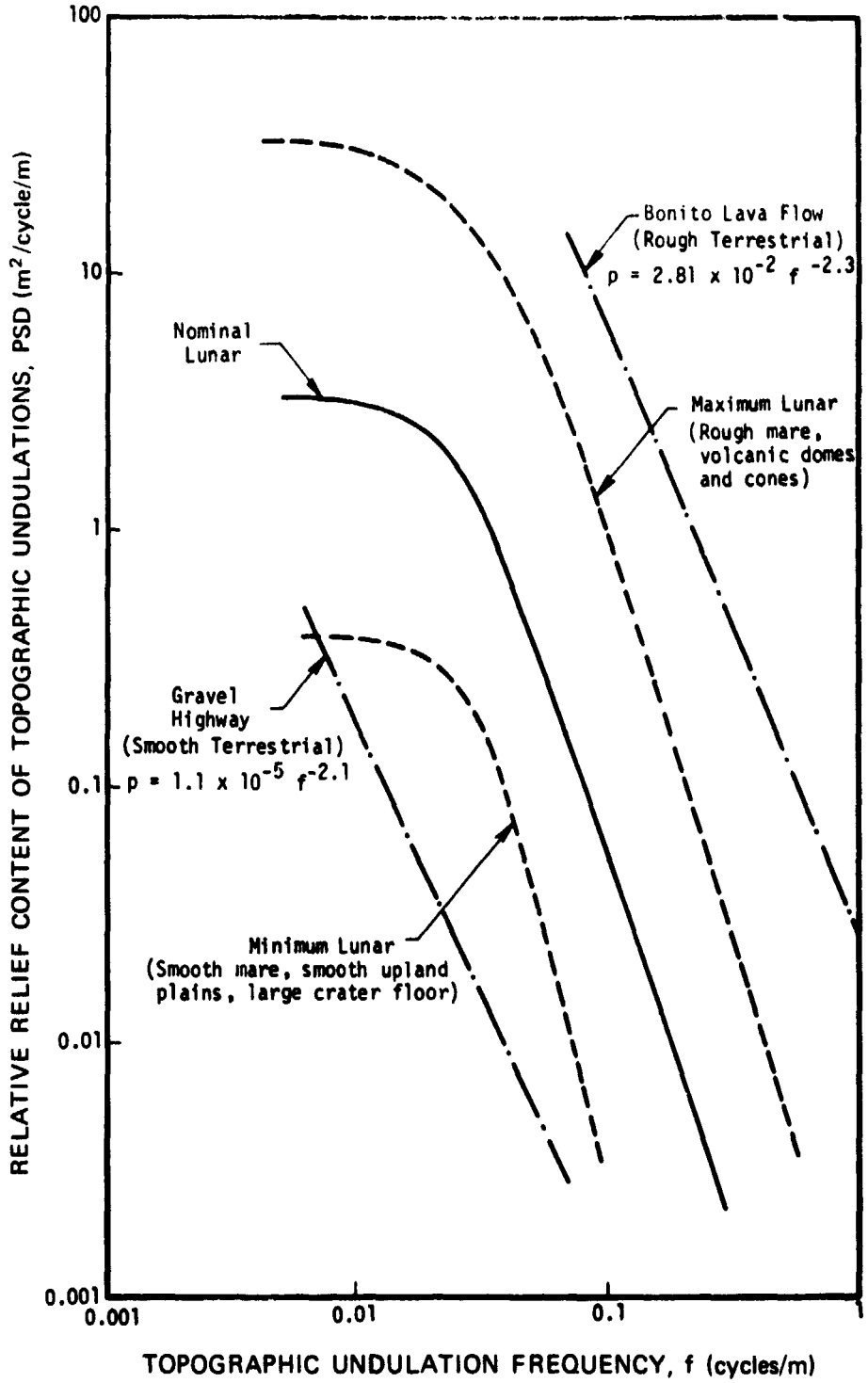

Figure 9. – Surface Roughness – Power Spectral Density vs. Surface Wave Frequency (R. J. Pike, USGS).

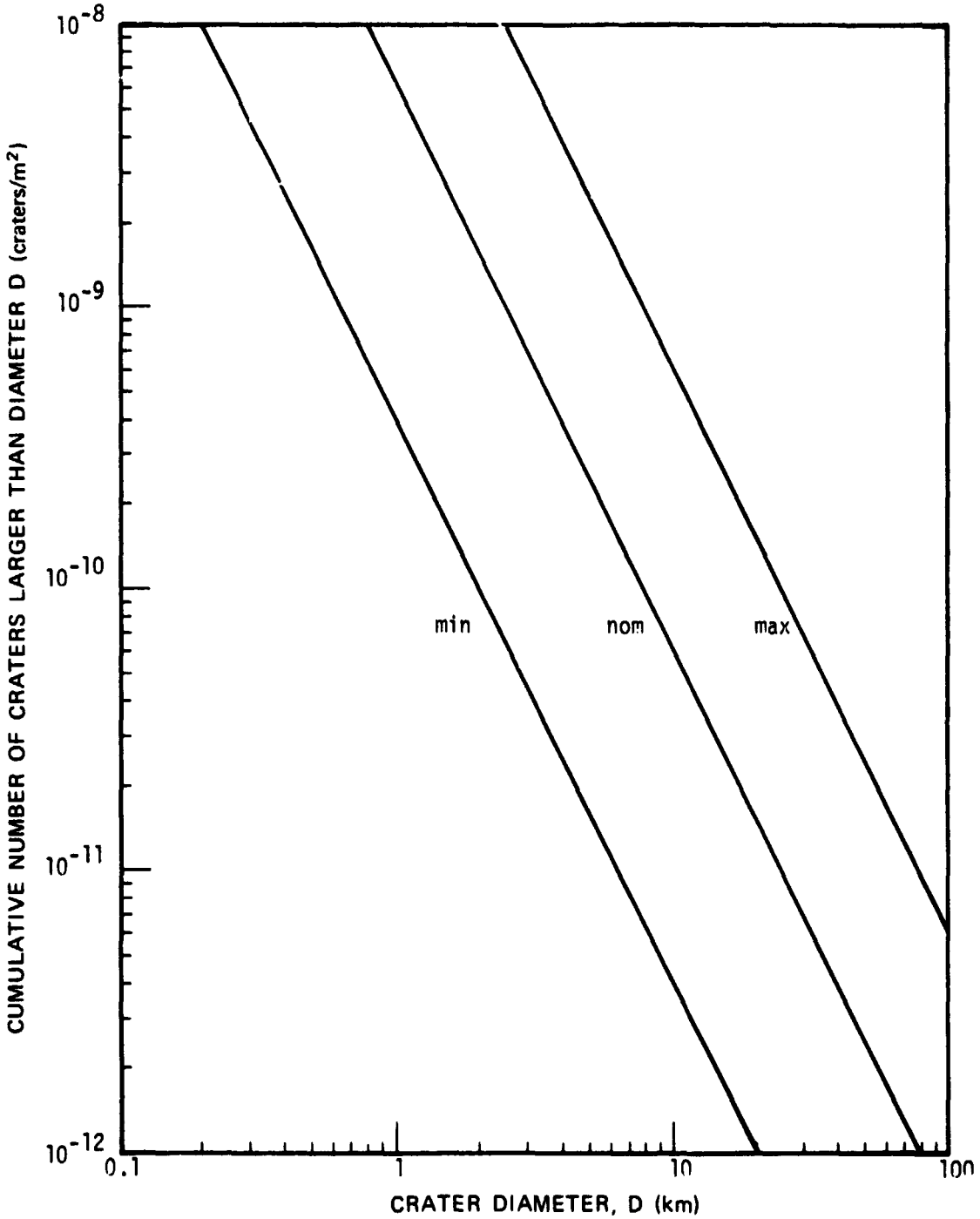

Figure 10. – Cumulative Number of Craters.

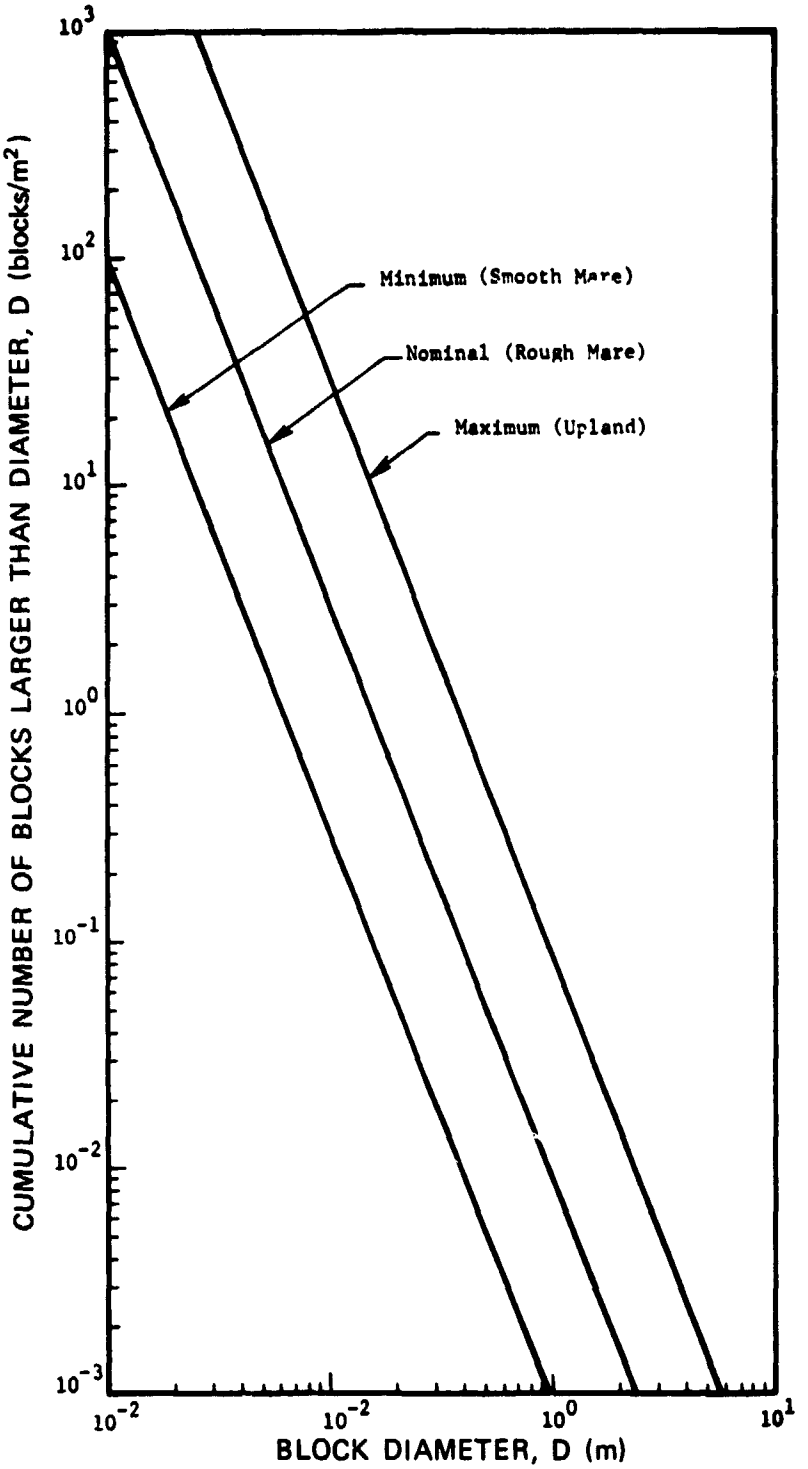

Figure 11. – Cumulative Number of Blocks

3.7 Soil Properties

3.7.1 Composition

The near-surface materials of Mars can be considered to be basaltic in composition with 60 ± 10 percent SiO_2 except where there are extensive deposits of carbon dioxide. Reflectivity data indicates that the surface contains varying amounts of limonite, hematite, geothite, montmorillonite and other impurities through chemical weathering and oxidation of the basalt.

3.7.2 Soil Models

Martian data imply the surface contains a variety of soil types just as on Earth. As a result, five different models are used to encompass the possible types of Martian soils.

The nominal Martian soil is considered to be the same as the average lunar soil. The four additional soil models are: loess, dune sand, lag gravel, and hard rock. Combinations of these five models may exist. For example, a layer of loess or sand overlaying rock. Recommended values for selected soil parameters are listed in table 3 for the five soil models. Cumulative particle size distributions are shown in figure 12.

3.7.3 Soil Penetration Resistance

The penetration resistance of the lunar nominal soil ranges from about 1 to 6 $N/cm^2/cm$ (ref. 97). The lower limit of this range can be considered to be representative of Martian loess and the upper limit to be representative of dune sand.

On the basis of theories like those in reference 141, estimates of the soil static bearing capacity of the soil can be made with the soil parameters listed in table 3. (The static bearing capacity of the soil generally has the characteristic that a small additional load suddenly produces a large increase in penetration.)

3.7.4 Moisture Content

Although Martian data clearly indicate the presence of water vapor in the atmosphere, it is not expected that liquid water will be common or necessarily exist on the surface. The most likely location of liquid water, although theoretically not stable, would be in thermally-protected areas such as caves, fissures, and voids in the Martian soil where the temperature is above freezing and the total ambient pressure is greater than the equilibrium vapor pressure at that temperature.

Exchange of moisture between the atmosphere and surface material is expected. Laboratory and theoretical studies suggest that surface material may contain up to ½ of 1 percent by weight of H_2O.*

*F. P. Fanale and W. A. Cannon, "H_2O and CO_2 Exchange on Mars . . .", J. Geophys. Res., vol. 79, no. 24, 1974, pp. 3397-3402.

Table 3
Parameters of Martian Soil Models

Parameter	Soil Model				
	Nominal	Loess	Dune Sand	Lag Gravel	Rock
Bulk Density, ρ (g/cm^3)	1.35 to 1.8	0.7 to 1.6	1.4 to 1.7	1.4 to 1.7	2.7 to 3.2
Porosity (percent)	48 ± 8	56 ± 10	49 ± 5	49 ± 5	0 to 3
Cohesion (N/cm^2)	0.003 to 0.21	0 to 10	0 to 0.01	0	1000 to 5000
Angle of Internal Friction (deg)	35 to 45	25 to 41	30 to 40	30 to 40	40 to 50
Permeability (cm^2)	10^{-8} to 10^{-7}	10^{-8} to 10^{-6}	10^{-6} to 10^{-3}	10^{-3} to 10^{-1}	10^{-10}
Thermal Inertia, I (10^{-3} cal/cm^2 s$^{1/2}$ K)	1.2 to 2.0	4.5	6.0	10	20
Dielectric Constant	2.3 to 3.5	1.6 to 3.0	2.6 to 3.2	2.6 to 3.2	7.2 to 13

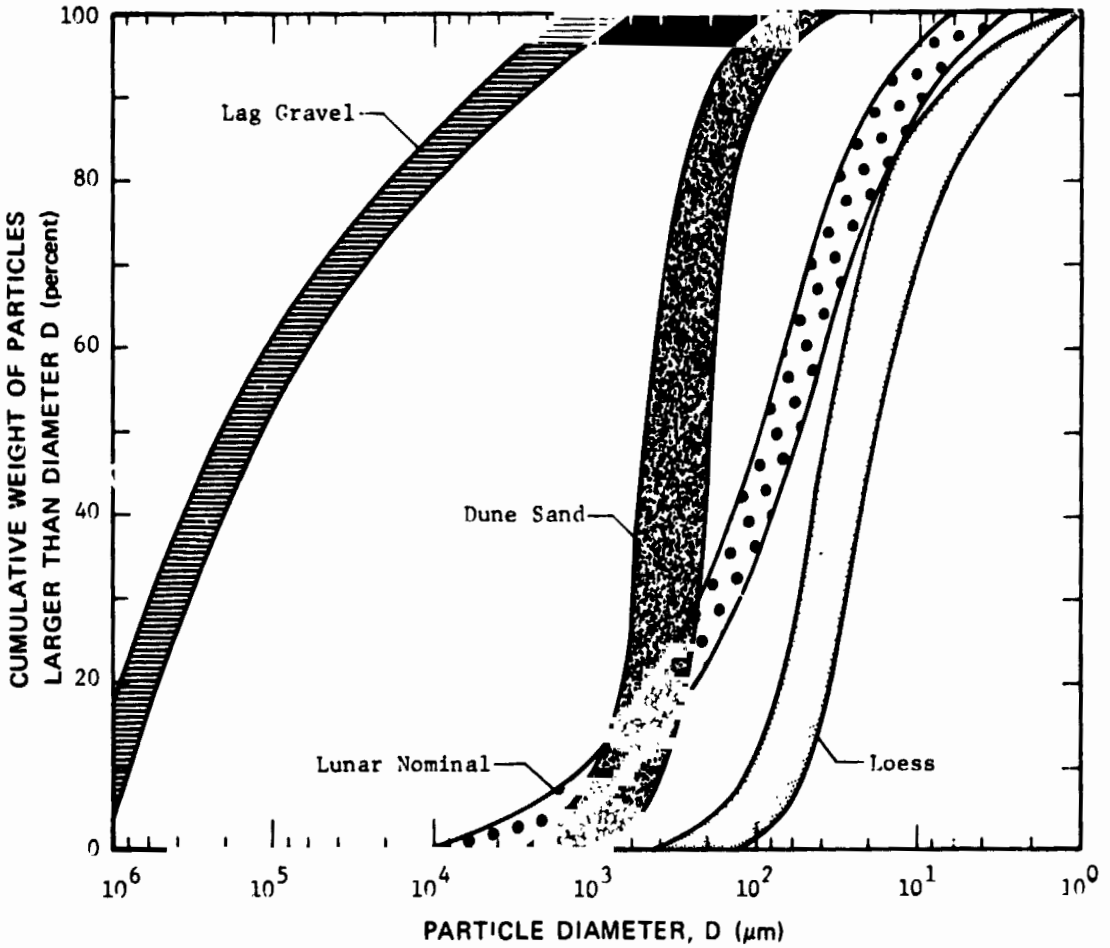

Figure 12. – Particle Size Distribution of Soil Models

3.8 Thermal Properties

3.8.1 Surface Temperature

The theoretical annual variation of minimum and maximum surface temperatures over the entire planet are shown in figures 13 and 14. The temperatures were computed from a mathematical model developed by H. H. Kieffer* from thermal properties and temperatures based on Martian data. No attempt was made in the development of the model to represent temperature gradients precisely at the edge of the polar cap. As a result, the large temperature changes at the polar cap boundaries are only representative of the actual temperature variation. Figures 13 and 14 correspond to an emissivity $\epsilon = 1.00$, bolometric albedo $A_{bol} = 0.25$ and thermal inertia $I = 0.0065$ cal/cm^2 $S^{1/2}$ K. The variation of minimum and maxi-

*Figures 13 through 17 were developed by Hugh H. Kieffer of UCLA; this work was used in establishing engineering models for the Viking Project.

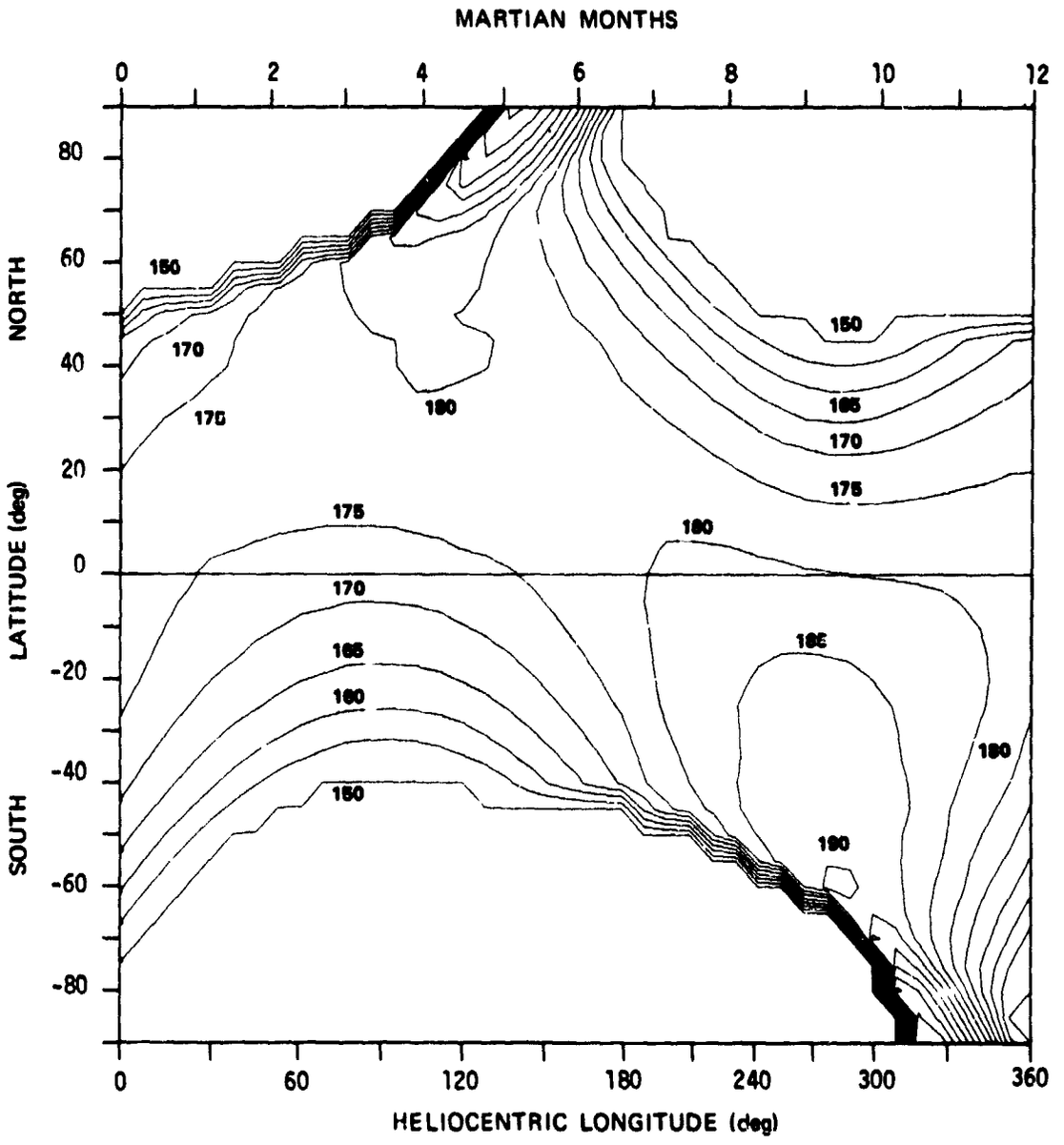

Figure 13. – Annual Variation of Minimum Global Surface Temperature in Degrees K for $I = 0.0065$ cal/cm^2 s$^{1/2}$ K, $A_{bol} = 0.25$ and $\epsilon = 1.00$.

mum temperatures for other values of I, ϵ, and A_{bol} can be estimated from the diurnal variations of surface temperature shown in figures 15 and 16.

Figure 15* shows the diurnal temperature variation at the equator for four values of thermal inertia for $\epsilon = 1.00$ and $A_{bol} = 0.25$ when Mars is at a zero heliocentric longitude. Figure 16

*Figures 13 through 17 were developed by Hugh H. Kieffer of UCLA; this work was used in establishing engineering models for the Viking Project.

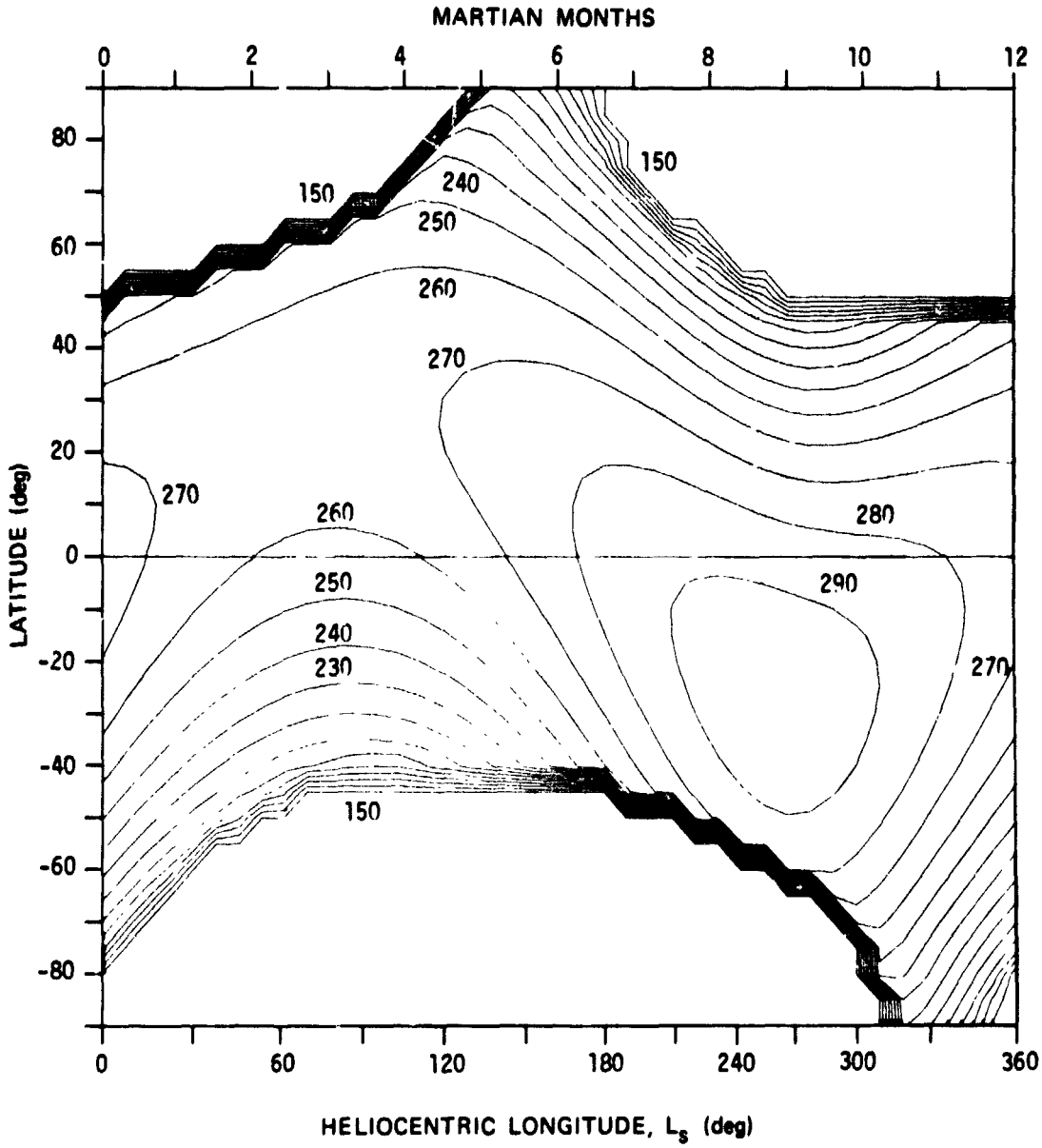

Figure 14. – Annual Variation of Maximum Global Surface Temperature in Degrees K for I = 0.0065 cal/cm^2 s$^{1/2}$ K, A_{bol} = 0.25 and ϵ = 1.00.

shows the diurnal temperature variation corresponding to the 0.0065 thermal inertia curve in figure 15 when ϵ ranges between 0.90 and 1.00 and A_{bol} ranges between 0.25 and 0.35. The upper boundary corresponds to A_{bol} = 0.25, ϵ = 0.90, while the lower boundary corresponds to A_{bol} = 0.35, ϵ = 1.00.

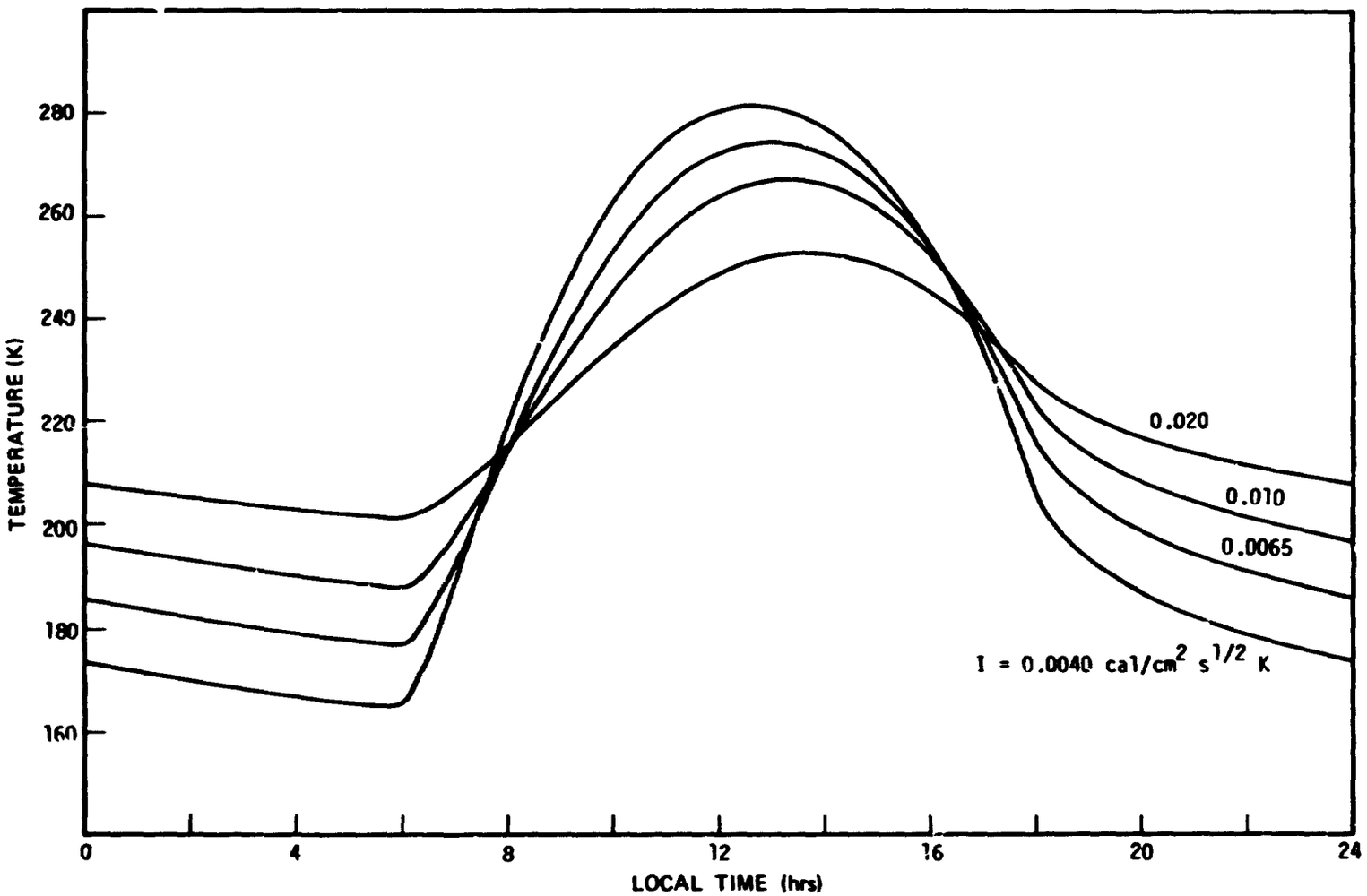

Figure 15. — Influence of Thermal Inertia on Equatorial Surface Temperature for the Beginning of Northern Spring, $A_{bol} = 0.25$ and $\epsilon = 1.00$.

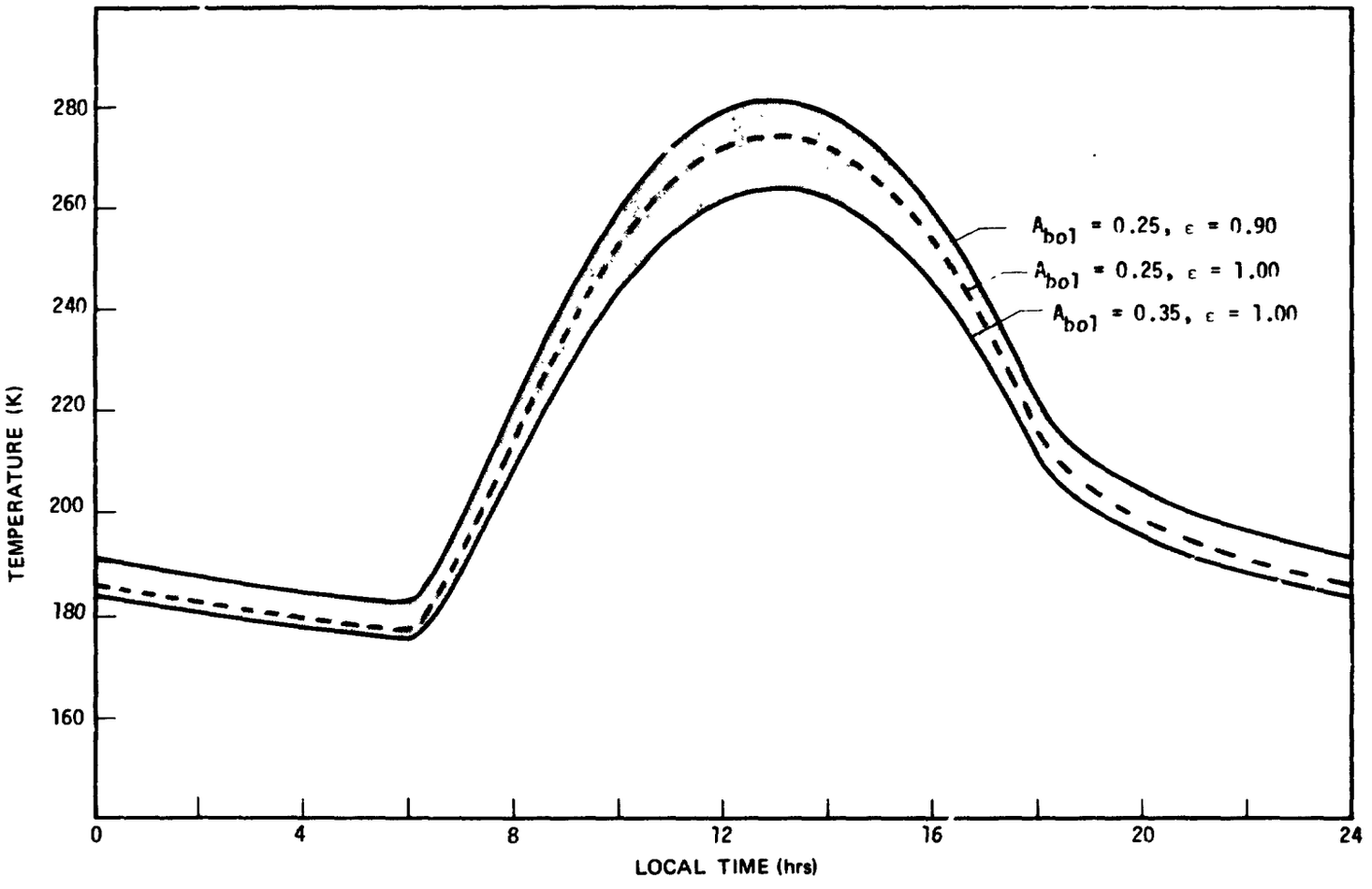

Figure 16. — Influence of Bolometric Albedo and Emissivity on Equatorial Surface Temperature for the Beginning of Northern Spring, Thermal Inertia = 0.0065 cal/cm^2 s$^{1/2}$ K.

3.8.2 Subsurface Temperature

The variation of subsurface temperature along the equator is shown in figure 17* for the first 15 cm of depth. These temperatures correspond to I = 0.0065 cal/cm^2 S$^{1/2}$ K, ϵ = 1.00, A_{bol} = 0.25.

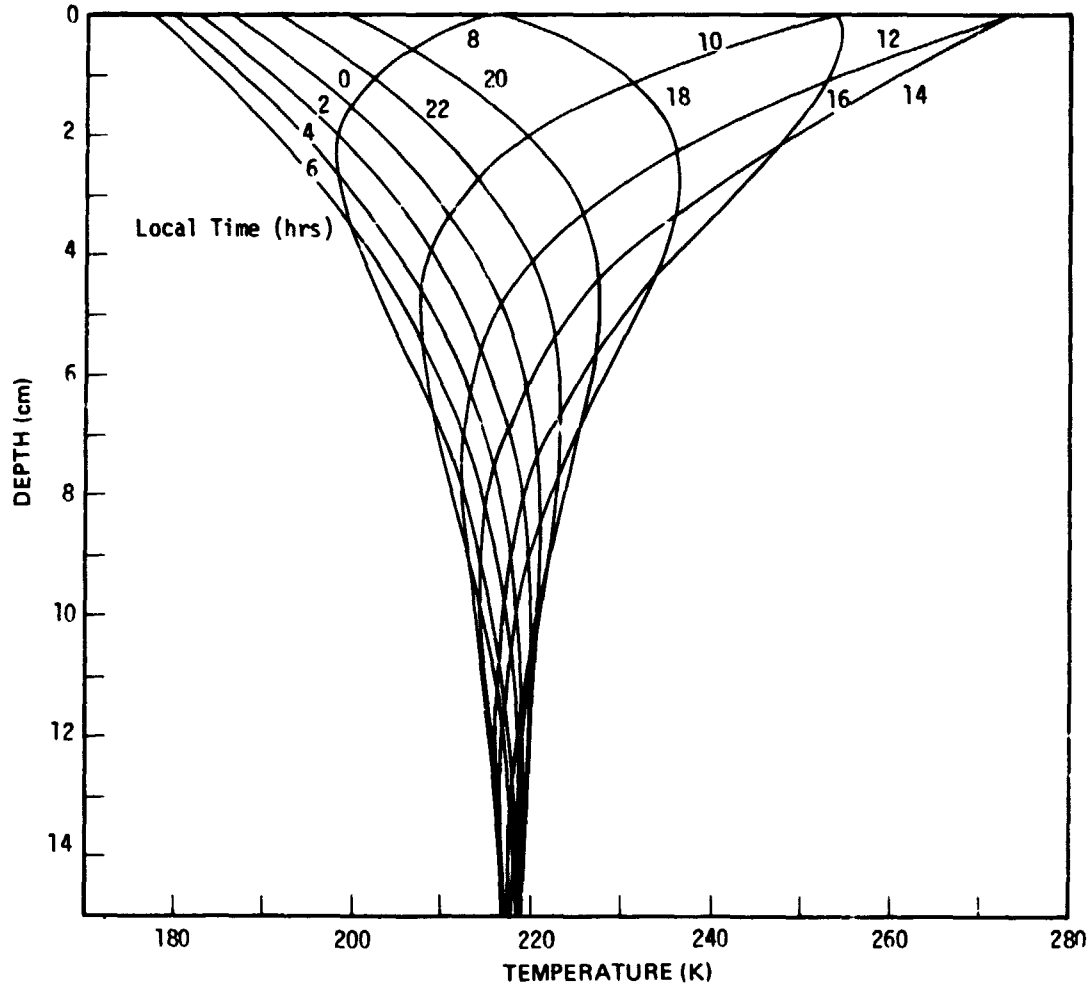

Figure 17. – Equatorial Subsurface Temperature for the Beginning of Northern Spring, I = 0.0065 cal/cm^2 s$^{1/2}$ K, A_{bol} = 0.25 and ϵ = 1.00.

*Figures 13 through 17 were developed by Hugh H. Kieffer of UCLA; this work was used in establishing engineering models for the Viking Project

3.8.3 Thermal Parameters

Recommended values for the Martian surface thermal parameters are listed in table 4.

Table 4
Thermal Parameters

Parameter	Value
Thermal Conductivity, k (cal/s cm K)	2×10^{-5} to 2×10^{-4}
Specific Heat, c (cal/g K)	0.15 to 0.19
Emissivity, ϵ (dimensionless)	0.90 to 0.98
Thermal Inertia, I (10^{-3} cal/cm^2 s$^{1/2}$ K)	4 to 10
Bolometric Albedo, A_{bol} (dimensionless)	0.2 to 0.4

3.9 Electrical Properties

3.9.1 Dielectric Constant

Ranges for the dielectric constant ϵ, and loss tangent, tan δ, are given in table 5.

Table 5
Electrical Properties of Soil and Rocks

Parameter	Value	
	Soil	Rocks
Dielectric constant, ϵ	1 to 3	7 to 9
Loss tangent, tan δ	0.005 to 0.05	0.01 to 0.10

3.10 Optical Properties

The surface spectral radiance is expressed in reference 61 as

$$N_\lambda = \frac{1}{\pi} E_S \tau_\lambda(i;\gamma)\tau_\lambda(e;\gamma)\rho_o \, \Phi(i,e,\alpha)$$

where

N = surface spectral radiance (watts/cm^2 − steradian)
E_S = solar irradiance at Mars (watts/cm^2)
$\tau_\lambda(i;\gamma)$ = spectral transmission of atmosphere = exp ($-\gamma$/cos i) (dimensionless)
$\tau_\lambda(e;\gamma)$ = spectral transmission of atmosphere = exp ($-\gamma$/cos e) (dimensionless)
ρ_o = surface normal spectral albedo (dimensionless)
γ = atmospheric optical thickness (dimensionless)

The photometric function $\Phi(i,e,\alpha,\lambda)$ is given in section 3.10.2 in terms of the angles shown in figure 18. In the figure, i and e are the angles of incidence and emergence measured between the surface normal line and the incidence and emergence rays, respectively, and α is the angle in the plane containing the incident and emitted rays (the phase plane). The great circle passing through the point N, and perpendicular to the phase plane, intercepts the phase plane at N′. The two factors τ_λ (i;γ) and τ_λ (e;γ) account for the loss of light through the atmosphere. If the point of observation is on the surface. the factor exp ($-\gamma$/cos e) is set equal to unity. Observations from orbit require both factors to account for the loss in the incident and emergence light rays. Recommended values for the optical thickness γ are listed in reference 61 over the wavelength range 0.25 to 0.50 μm. The values listed imply γ = 0.006 ± 0.004 is a reasonable range for the wavelength range of validity of the photometric function given in section 3.10.1.

3.10.1 Photometric Function

The photometric function (valid over the approximate range λ = 0.42 to 0.70 μm) is expressed in terms of the angles shown in figure 18 as

$$\Phi(i,e,\alpha) = \frac{\cos i}{(1 + a_0 + a_1)(\cos i + \cos e)} \left[(1 + a_0 \cos \alpha)\, f\,(i,e,\alpha;a_2) + a_1(\cos i + \cos e)\right]$$

where $a_0 = 0.55$, $a_1 = 0.60$, $a_2 = 0.18$ are empirical parameters that depend on properties of the surface, and where

$$f(i,e,\alpha;a_2) = e^{\mu-\nu} + \nu\int_0^1 \exp\left\{\mu - \frac{\nu}{6\pi g}\left[3\pi(2g-1)x + 6x\sin^{-1}x + 2(2+x^2)(1-x^2)^{1/2}\right]\right\} dx$$

in which

$$\mu = \frac{4a_2(1+\cos\alpha)}{3\sin\alpha}$$

$$\nu = \frac{\pi a_2(\cos i + \cos e)[\cos\delta + \cos(\alpha-\delta)]\cos\psi}{\sin\alpha\cos i\cos e}$$

$$g = \frac{(\cos i + \cos e)\cos\delta\cos(\alpha-\delta)\cos\psi}{[\cos\delta + \cos(\alpha-\delta)]\cos i\cos e}$$

$$\cos\alpha = \cos i\cos e + \sin i\sin e\cos\phi$$

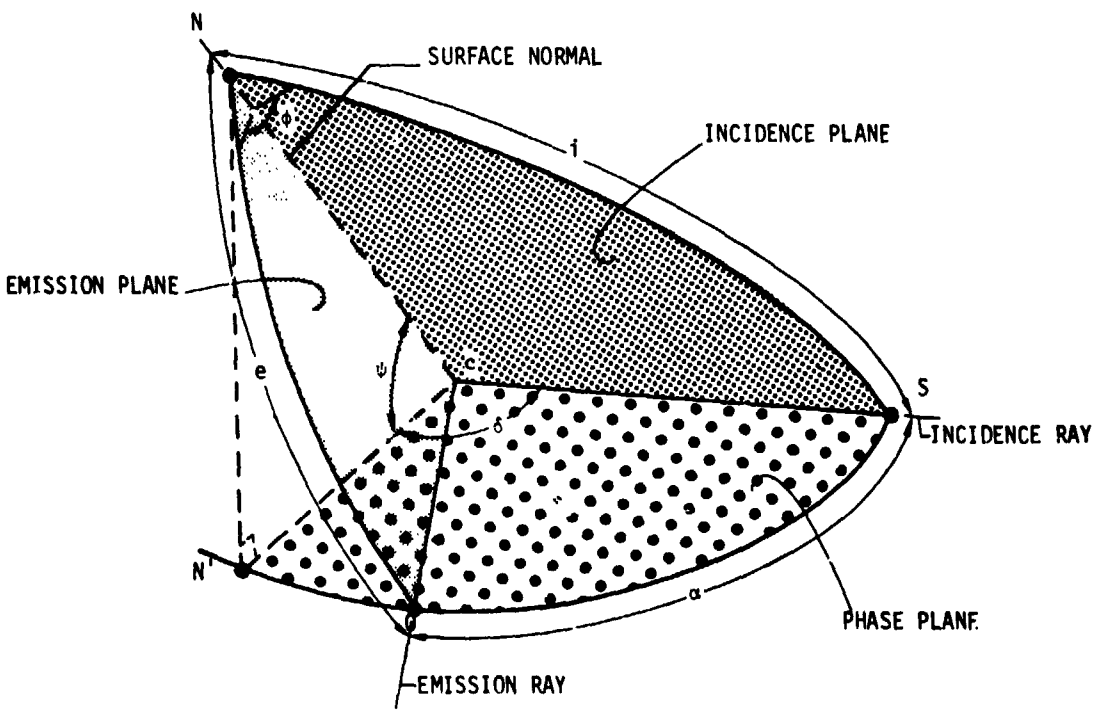

Figure 18. – Geometrical Parameters in Photometric Function.

3.10.2 Albedo

Spectral albedo values are listed in table 6 and plotted in figure 19.

Table 6
Estimated Surface Normal Spectral Albedo for Desert and Mare Areas
(ref. 61)

Wavelength λ (μm)	Normal Spectral Albedo, ρ_o			
	Mare		Desert	
	Dark Area	Average	Average	Bright Area
0.40	0.06	0.06	0.06	0.07
0.45	0.07	0.07	0.07	0.09
0.50	0.08	0.09	0.10	0.13
0.55	0.09	0.11	0.14	0.20
0.60	0.11	0.14	0.20	0.28
0.65	0.13	0.17	0.25	0.35
0.70	0.14	0.19	0.28	0.38
0.75	0.14	0.20	0.30	0.39
0.80	0.14	0.21	0.30	0.40
0.85	0.13	0.21	0.30	0.40
0.90	0.12	0.21	0.30	0.40
0.95	0.12	0.21	0.30	0.40
1.00	0.12	0.20	0.30	0.40

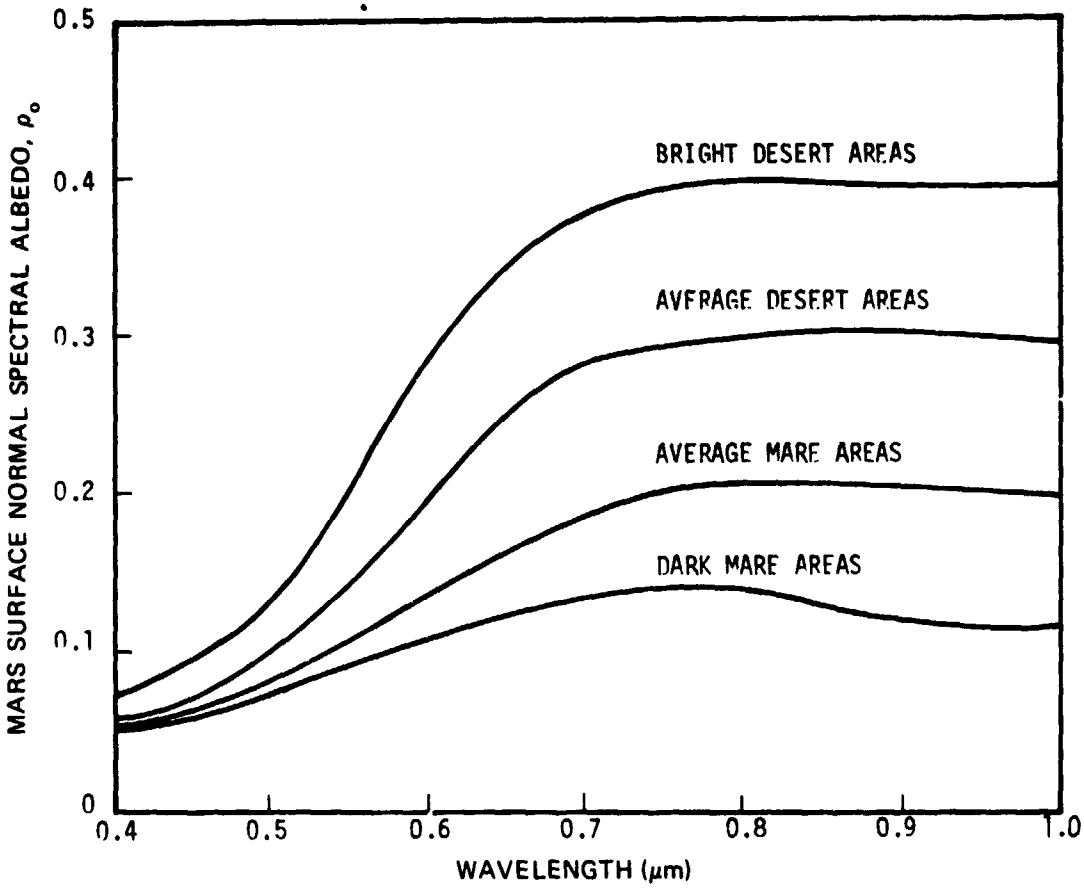

Figure 19. – Estimates of Mars Surface Normal Spectral Albedo (from Binder, Ref. 61).

REFERENCES

1. Anon.: Mars Surface Models, NASA SP-8020, May, 1969.

2. Baum, W. A.; Millis, R. L.; Jones, S. E.; and Martin, L. J.: The International Planetary Patrol Programs, Icarus, Vol. 12, 1970, pp. 435-439.

3. Opik, E. J.: The Martian Surface, Science, Vol. 153, No. 3733, 1966, pp. 255-265.

4. Dollfus, A.: Visual and Photographic Studies of Planets at the Pic du Midi, The Solar System, Vol. III, Planets and Satellites, edited by G. Kuiper and B. M. Middlehurst, 1961, pp. 534-571.

5. de Vaucouleurs, G.: The Physical Ephemeris of Mars, Icarus, Vol. 3, 1964, pp. 236-247.

6. Focas, J. H.: Etude photometrique et polarimetrique des phenomenes saisonniers de la planete Mars, Ann. d'Astrophysique, Vol. 29, 1961, pp. 309-325.

7. Inge, J. L.; Capen, C. F.; Martin, L. J.; Faure, B. Q.; and Baum, W. A.: A New Map of Mars from Planetary Patrol Photographs, Sky and Telescope, Vol. 41, No. 6, June 1971, pp. 336-339.

8. de Vaucouleurs, G.; Davies, M. E.; and Sturms, F. M., Jr.: Mariner 9 Areographic Coordinate System, JGR, Vol. 78, No. 20, 1973, pp. 4395-4404.

9. Davies, M. E., and Arthur, D. W. G.: Martian Surface Coordinates, JGR, Vol. 78, No. 20, 1973, pp. 4355-4394.

10. Batson, R. B.: Cartographic Products from the Mariner 9 Mission, JGR, Vol. 78, No. 20, 1973, pp. 4424-4435.

11. de Vaucouleurs, G.; Roth, J.; and Mulholland, C.: Preliminary Albedo Map of the South Polar Region, JGR, Vol. 78, No. 20, 1973, pp. 4436-4439.

12. Dollfus, A.: Etude des planetes par la polarisation de leur lumier, Ann. d'Astrophysique, Suppl. No. 4, 1947, p. 114.

13. Dollfus, A.: Etude de la planete Mars de 1954 a 1958, Ann. d'Astrophysique, Vol. 28, 1965, pp. 722-747.

14. Dollfus, A.: Proprietes photometrique des contress desertiques sur la planete Mars, Comptes Rendus, Vol. 244, 1957, pp. 162-164.

15. Kellermann, K. I.: The Thermal Radio Emission from Mercury, Venus, Mars, Saturn, and Uranus, Icarus, Vol. 5, 1966, pp. 478-490.

16. Kieffer, H. H.; Chase, S. C.; Miner, E.; Münch, G.; and Neugebauer, G.: Preliminary Report on Infrared Radiometric Measurements from the Mariner 9 Spacecraft, JGR, Vol. 78, No. 20, 1973, pp. 4291-4312.

17. de Vaucouleurs, G.: Physics of the Planet Mars, Faber and Faber Limited, London, 1953.

18. Sagan, C.; Phaneuf, J. P.; and Ihnat, M.: Total Reflection Spectrophotometry and Thermogravimetric Analysis of Simulated Martian Surface Materials, Icarus, Vol. 4, 1965, pp. 43-61.

19. Michaux, C. M., and Newburn, R. L., Jr.: Mars Scientific Model, JPL Document No. 606-1, March 1, 1972.

20. Anon.: Radar Astronomy, edited by J. V. Evans and T. Hagfors, McGraw-Hill Book Co., New York, 1968.

21. Goldstein, R. M., and Gillmore, W. F.: Radar Observations of Mars, Science, Vol. 141, 20 September 1963, pp. 1171-1172.

22. Kotelnikov, W. A.; Dubrovnin, W. M.; Dubinskij, B. A.; Kislik, M. D.; Kusnezov, B. I.; Petrov, G. M.; Rabotjagov, A. P.; Rshiga, O. N.; and Schachovskaj, A. M.: Radar Studies of the Planet Mars in the Soviet Union, Sov. Phys-Dokl, Vol. 8, No. 8, February 1964, pp. 760-763, (Translation of 1963 article).

23. Goldstein, R. M.: Mars: Radar Observations, Science, Vol. 150, 1965, pp. 1715-1717.

24. Dyce, R. B.; Pettengill, G. H.; and Sanchez, A. D.: Radar Observations of Mars and Jupiter at 70 cm," The Astron. J., Vol. 72, No. 6, August 1967, pp. 771-781.

25. Pettengill, G. H.; Counselman, C. C.; Rainville, L. P.; and Shapiro, I. I.: Radar Measurements of Martian Topography, The Astron. J., Vol. 74, No. 3, April 1969, pp. 461-482.

26. Pettengill, G. H.; Rogers, A. E. E.; and Shapiro, I. I.: Martian Craters and Scarps as Seen by Radar, Science, Vol. 174, No. 4016, 1971, pp. 1321-1324.

27. Pettengill, G. H.; Shapiro, I. I.; and Rogers, A. E. E.: Topography and Radar Scattering Properties of Mars, Icarus, Vol. 18, 1973, pp. 22-28.

28. Downs, G. S.; Goldstein, R. M.; Green, R. R.; Morris, G. A.; and Reichley, P. E.: Martian Topography and Surface Properties as Seen by Radar: The 1971 Opposition, Icarus, Vol. 18, 1973, pp. 8-21.

29. Downs, G. S.; Goldstein, R. M.; Green, R. R.; Morris, G. A.: Mars Radar Observations, a Preliminary Report, Science, Vol. 174, No. 4016, 24 December 1971, pp. 1324-1327.

30. Sagan, C.; Pollack, J. B.; and Goldstein, R. M.: Radar Doppler Spectroscopy of Mars, I. Elevation Differences between Bright and Dark Areas, The Astron. J., Vol. 72, No. 1, February 1967, pp. 20-34.

31. Glasstone, S., The Book of Mars, NASA SP-179, 1968.

32. Binder, A. B.: Topography and Surface Features of Mars, Icarus, Vol. 11, 1969, pp. 24-35.

33. Anon.: Mariner-Mars 1964 Final Project Report, NASA SP-139, 1967.

34. Nicks, O. W.: A Review of the Mariner IV Results, NASA SP-130, 1967.

35. Leighton, R. B.; Murray, B. C.; Sharp, R. P.; Allen, J. D.; and Sloan, R. K.: Mariner Mars 1964 Project Report: Television Experiment, Part I, Investigators Report, Mariner IV Pictures of Mars, JPL TR 32-884, December 15, 1967.

36. Hanel, R. A.; Conrath, B. J.; Hovis, W. A.; Kunde, V. G.; Lowman, P. D.; Pearl, J. C.; Probhakara, C.; Schlachman, B.; and Levin, G. V.: Infrared Spectroscopy Experiment on the Mariner 9 Mission: Preliminary Results, Science, Vol. 175, 1972, pp. 305-308.

37. Horn, D.; McAfee, J. M.; Winer, A. M.; Herr, K. C.; and Pimentel, G. C.: The Composition of the Martian Atmosphere: Minor Constitutents, Icarus, Vol. 16, 1972, pp. 543-556.

38. Owen, T., and Sagan, C.: Minor Constituents in Planetary Atmospheres: Ultraviolet Spectroscopy from Orbiting Astronomical Observatory, Icarus, Vol. 16, 1972, pp. 557-568.

39. Anon.: Mariner Mars 1971 Project Final Report, Volume II. Preliminary Science Results, JPL TR 32-1550, February 1, 1972.

40. Conrath, B.; Curran, R.; Hanel, R.; Kunde, V.; Maguire, W.; Pearl, J.; Pirraglia, J.; and Welker, J.: Atmospheric and Surface Properties of Mars Obtained by Infrared Spectroscopy on Mariner 9, JGR, Vol. 78, No. 20, 1973, pp. 4267-4278.

41. Miyamoto, S., and Hattori, A.: Polar Cap of Mars, Icarus, Vol. 9, 1968, pp. 440-445.

42. Wade, F. A., and DeWys, J. N.: Permafrost Features on the Martian Surface, Icarus, Vol. 9, 1968, pp. 175-185.

43. Schorn, R. A.; Farmer, C. B.; and Little, S. J.: High-Dispersion Spectroscopic Studies of Mars, III. Preliminary Results of 1968-1969 Water-Vapor Studies, Icarus, Vol. 11, 1969, pp. 283-288.

44. Hanel, R.; Conrath, B.; Hovis, W.; Kunde, V.; Lowman, P.; Maguire, W.; Pearl, J.; Pirraglia, J.; Prabhakara, C.; Schlachman, B.; Levin, G.; Straat, P.; and Burke, T.: Investigation of the Martian Environment by Infrared Spectroscopy on Mariner 9, Icarus, Vol. 17, 1972, pp. 423-442.

45. Curran, R. J.; Conrath, B. J.; Hanel, R. A.; Kunde, V. G.; and Pearl, J. C.: Mars: Mariner 9 Spectroscopic Evidence for H_2O Ice Clouds, Science, Vol. 182, 1973, pp. 381-383.

46. Houck, J. R.; Pollack, J. B.; Sagan, C.; Schaack, D.; and Decker, J. A., Jr.: High Altitude Infrared Spectroscopic Evidence for Bound Water on Mars, Icarus, Vol. 18, 1973, pp. 470-480.

47. Leovy, C. B.; Briggs, G. A.; and Smith, B. A.: Mars Atmosphere During the Mariner 9 Extended Mission: Television Results, JGR, Vol. 78, No. 20, 1973, pp. 4252-4266.

48. Milton, D. J.: Water and Process of Degradation in the Martian Landscape, JGR, Vol. 78, No. 20, 10 July 1973, pp. 4037-4047.

49. Sharp, R. P.: Mars: South Polar Pits and Etched Terrain, JGR, Vol. 78, No. 20, 10 July 1973, p. 4222.

50. Cutts, J. A.: Nature and Origin of Layered Deposits of the Martian Polar Regions, JGR, Vol. 78, No. 20, 10 July 1973, p. 4231.

51. Cutts, J. A.: Wind Erosion in the Martian Polar Regions, JGR, Vol. 78, No. 20, 10 July 1973, p. 4211.

52. Smith, S. A.; and Smith B. A.: Diurnal and Seasonal Behavior of Discrete White Clouds on Mars, Icarus, Vol. 16, 1972, pp. 509-521.

53. Baum, W. A.: The International Planetary Patrol Program; An Assessment of the First Three Years," to appear in Planetary and Space Science.

54. Sagan, C.; Veverka, J.; and Gierasch, P.: Observational Consequences of Martian Wind Regimes, Icarus, Vol. 15, 1971, pp. 253-278.

55. Boyce, P. B., and Thompson, D. T.: A New Look at the Martian Violet Haze Problem I. Syrtis Major-Arabia, 1969, Icarus, Vol. 16, 1972, p. 291.

56. Boyce, P.: Remote Sensing Photometric Studies of Mars in 1971, Icarus, Vol. 18, 1973, pp. 134-141.

57. Blumsack, S. L.: On the Effects of Large-Scale Temperature Advection in the Martian Atmosphere, Icarus, Vol. 15, 1971, pp. 429-442.

58. Gifford, F. A.: A Study of Martian Yellow Clouds that Display Movement, Monthly Weather Rev., Vol. 92, No. 10, 1964, pp. 435-440.

59. Bagnold, R. A.: The Physics of Blown Sand and Desert Dunes, Methuen & Co., Ltd., London, Second printing, 1965.

60. Gierasch, P., and Sagan, C.: A Preliminary Assessment of Martian Wind Regimes, Icarus, Vol. 14, 1971, pp. 312-318.

61. Anon., Mars Engineering Model, Viking 75 Project Report M75-125-3, 4 January 1974.

62. Koval, I: Toward the Red Planet Again, Pravda, July 29, 1973.

63. Anon.: Space and Planetary Environment Criteria Guidelines for Use in Space Vehicle Development, 1971 Revision, NASA TM X-64627, 15 November 1971.

64. Golitsyn, G. S.: On the Martian Dust Storm, Icarus, Vol. 18, 1973, pp. 113-119.

65. Pollack, J. B., and Sagan, C.: An Analysis of Martian Photometry and Polarimetry, Space Sci. Rev., Vol. 9, 1969, pp. 243-299.

66. Otterman, J.; and Bronner, F. E.: Martian Wave of Darkening: A Frost Phenomenon, Science 153, 1966, pp. 56-60.

67. Richardson, R. S.; and Bonestell, C.: Mars, Harcourt Brase and World Inc., New York, 1964.

68. Sagan, C., and Pollack, J. B.. Windblown Dust on Mars, Nature, Vol. 223, 1969, pp. 791-794.

69. Sharp, R. P.: Surface Processes Modifying Martian Craters, Icarus, Vol. 8, 1968, pp. 472-480.

70. Adlon, G. L.; Weinberger, R. K.; and McClure, D. R.: Martian Sand and Dust Storm Simulation and Evaluation, NACA CR-66882, 31 October 1969.

71. Weinberger, R. K.; and Adlon, G. L.: Particle Dislodgement and Entrainment by a Low Density Airstream Flowing Over a Surface, NACA CR 111924, 6 August 1971.

72. Wood, G. P.; Weaver, W. R.; and Henry, R. M.: The Minimum Free Stream Wind Speed for Initiating Motion of Surface Materials on Mars, NASA-Langley Research Center, submitted for publication in 1973.

73. Greeley, R.; Iversen, J. D.; Pollack, J. B.; Udovich, N.; and White, B.: Wind Tunnel Studies of Martian Aeolian Processes, NASA TM X-62, 297, May 1973.

74. Dollfus, A.: Polarization Studies of Planets, The Solar System, Vol. III, Planets and Satellites, edited by G. Kuiper and B. M. Middlehurst, 1961, pp. 343-399.

75. Ingersoll, A. P.: Polarization Measurements of Mars and Mercury: Rayleigh Scattering in the Martian Atmosphere, The Astrophys. J., Vol. 163, January 1, 1971, pp. 121-129.

76. Anon.: Mariner-Mars 1969 A Preliminary Report, NASA SP-225, November 1969.

77. Kliore, A. J.; Fjeldbo, G.; Seidel, B. L.; Sykes, M. J.; and Woiceshyn, P. M.: S-Band Radio Occultation Measurements of the Atmosphere and Topography of Mars with Mariner 9: Extended Mission Coverage of Polar and Intermediate Latitudes, JGR, Vol. 78, No. 20, 1973, pp. 4331-4351.

78. Michael, W. H., Jr.; Wallio, H. A.; and Levine, J. S.: Mars Lower Atmosphere: Some New Implications, presented at the XV Plenary Meeting of COSPAR, Madrid, Spain, Paper No. k.7, May 1972.

79. Sinton, W. M., and Strong, J.: Radiometric Observations of Mars, Astrophys. J., Vol. 131, No. 2, 1960, pp. 459-469.

80. Gifford, F., Jr.: The Surface-Temperature Climate of Mars, Astrophys. J., Vol. 123, 1956, pp. 154-161.

81. Mayer, C. H.; McCullough, T. P.; and Sloanaker, R. M.: Measurements of Planetary Radiation at Centimeter Wavelengths, Proc. of IRE, Vol. 46, No. 1, 1958, pp. 260-266.

82. Kuzmin, A. D.; Losovsky, B.Ya.; and Vetukhnovskaya, Yu. N.: Measurements of Mars Radio Emission at 8.22 mm and Evaluation of Thermal and Electrical Properties of its Surface, Icarus, Vol. 14, 1971, pp. 192-195.

83. Efanov, V. A.; Moiseev, I. G.; Kislyakov, A. G.; and Naumov, A. I.: Mars and Jupiter: Radio Emission at 2.3 mm and 8.15 mm," Icarus, Vol. 14, 1971, pp. 198-203.

84. Hobbs, R. W., and Knapp, S. L.: Planetary Temperatures at 9.55 mm Wavelength, Icarus, Vol. 14, 1971, pp. 204-209.

85. Janssen, M. A., and Welch, W. J.: Mars and Jupiter: Radio Emission at 135 cm, Icarus, Vol. 18, 1973, pp. 502-504.

86. Klein, M. J.: Mars: Measurements of Its Brightness Temperature at 1.85 and 3.75 cm Wavelength, Icarus, Vol. 14, 1971, pp. 210-213.

87. Epstein, E. E.: Mars: A Possible Discrepancy between the Radio Spectrum and Elementary Theory, Icarus, Vol. 14, 1971, pp. 214-221.

88. Sagan, C., and Veverka, J.: The Microwave Spectrum of Mars: An Analysis, Icarus, Vol. 14, 1971, pp. 222-234.

89. Ulich, B. L.; Cogdell, J. R.; and Davis, J. H.: Planetary Brightness Temperature Measurements at 8.6 mm and 3.1 mm Wavelengths, Icarus, Vol. 19, 1973, pp. 59-82.

90. Cuzzi, J. N., and Muhleman. D. O.: The Microwave Spectrum and Nature of the Subsurface of Mars, Icarus, Vol. 17, 1972, pp. 548-560.

91. Kieffer, H. H.: Martian Surface Temperature; Diurnal and Annual Behavior, Paper in preparation.

92. Morrison, D.; Sagan, C.; and Pollack, J. B.: Martian Temperatures and Thermal Properties, Icarus, Vol. 11, 1969, pp. 36-45.

93. Leovy, C.: Note on Thermal Properties of Mars, Icarus, Vol. 5, 1966, pp. 1-6.

94. Moroz, V. I., and Ksanfomaliti, L. V.: Preliminary Results of the Astro-Physical Observations of Mars from A15 Mars-3, Presented at COSPAR Meeting, Madrid, Spain, May 1972.

95. Marov, M. Y.: COSPAR Annual Reviews on the Results Provided by Space Probes for Mars Studies, Presented at COSPAR Meeting, Madrid, Spain, May 1972.

96. Marov, M. Ya., and Petrov, G. I.: Investigations of Mars from the Soviet Automatic Stations Mars 2 and 3, Icarus, Vol. 19, 1973, pp. 163-179.

97. Anon.: Lunar Surface Models, NASA SP-8023, September 1973.

98. Fountain, J. A., and West, E. A.: Thermal Conductivity of Particulate Basalt as a Function of Density in Simulated Lunar and Martian Environments, JGR, Vol. 75, No. 20, 10 July 1970, pp. 4063-4069.

99. Winter, D. F., and Saari, J. M.: A Particulate Thermophysical Model of the Lunar Soil, The Astrophysical Journal, Vol. 156, June 1969, pp. 1135-1151.

100. Troitskii, V,S.: The Possibility of Investigating Properties of Martian Soil through Its Radio Emission, Soviet Astronomy, Vol. 14, No. 2, September-October 1970, pp. 308-314.

101. Balsamo, S. R., and Salisbury, J. W.: Slope Angle and Frost Formation on Mars, Icarus, Vol. 18, 1973, pp. 156-163.

102. Hovis, W. W., Jr., and Callahan, W. R.: Infrared Reflectance Spectra of Igneous Rocks, Tuffs, and Red Sandstone from 0.5 to 22 μ, J. of the Optical Society of America, Vol. 55, No. 5, May 1966, pp. 639-643.

103. Lorell, J., and Shapiro, I. I.: The Mariner 9 Celestial Mechanics Experiment: A Status Report, JGR, Vol. 78, No. 20, 1973, pp. 4327-4329.

104. Lorell, J., et al: Gravity Field of Mars from Mariner 9 Tracking Data, Icarus, Vol. 18, 1973, pp. 304-316.

105. Jordan, J. F.; and Lorell, J.: Mariner 9, An Instrument of Dynamical Science, Presented at AAS/AIAA Astrodynamics Conference, Vail, Colorado, July 16-18, 1973.

106. Murray, B. C.; Soderblom, L. A.; Sharp, R. P.; and Cutts, J. A.: The Surface of Mars, 1. Cratered Terrains, JGR, Vol. 76, No. 2, 1971, pp. 313-330.

107. Sharp, R. P.; Soderblom, L. A.; Murray, B. C.; and Cutts, J. A.: The Surface of Mars, 2. Uncratered Terrains, JGR, Vol. 76, No. 2, 1971, pp. 331-342.

108. Carr, M. H.; Masursky, H.; and Saunders, R. S.: A Generalized Geologic Map of Mars, JGR, Vol. 78, No. 20, 1973, pp. 4031-4036.

109. Masursky, H.: An Overview of Geological Results from Mariner 9, JGR, Vol. 78, No. 20, 1973, pp. 4009-4030.

110. Hartmann, W. K.: Martian Cratering, IV: Mariner 9 Initial Analysis of Cratering Chronology, JGR, Vol. 78, No. 20, 1973, pp. 4096-4116.

111. Kliore, A. J.; et al.: The Atmosphere of Mars from Mariner 9 Radio Occultation Measurements. Icarus 17, 1972, pp. 484-516.

112. Masursky, H.; et al.: Mariner 9 TV Reconnaissance of Mars and Its Satellites: Preliminary Results. Science 175, 1972, pp. 294-304.

113. Parkinson, T. D.; and Hunten, D. M.: CO_2 Distribution on Mars. Icarus 18, 1973, pp. 29-53.

114. Cain, D. L.; et al.: The Shape of Mars from the Mariner 9 Occultations. Icarus 17, 1972, pp. 517-524.

115. Cain; et al.: Approximations to the Mean Surface of Mars and Mars Atmosphere Using Mariner 9 Occultations. Chapter 37 of Mariner Mars 1971 Project Final Report, vol. IV, July 15, 1973, pp. 495-498.

116. Pettengill, G. H.; Shapiro, I. I.; and Rogers, A. E. E.: Topography and Radar Scattering Properties of Mars. Icarus 18, 1973, pp. 22-28.

117. Marcus, A. H.: Distribution of Slopes on a Cratered Planetary Surface: Theory and Preliminary Applications, JGR, Vol. 74, No. 22, 1969, pp. 5253-5267.

118. Rowan, L. C.; McCauley, J. F.; and Holm, E. A.: Lunar Terrain Mapping and Relative-Roughness Analysis, Geological Survey Professional Paper 599-G, 1971.

119. Jaeger, R.,M., and Schuring. R. J.: Spectrum Analysis of Mare Cognitum, JGR, Vol. 71, No. 8, 1966, pp. 2023-2028.

120. Rozema, W.: The Use of Spectral Analysis in Describing Lunar Surface Roughness, Interagency Report: Astrogeology 12, U.S. Geological Survey, December 1968.

121. Aronson, J. R., and Emslie, A. G.: The Prospects for Mineral Analysis by Remote Infrared Spectroscopy, Lunar Geophysics, edited by Z. Kopal and D. Strangeway, D. Reidel Publ. Co., Boston, USA, 1972, pp. 594-606.

122. Salisbury, J. W., and Hunt, G. R.: Compositional Implications of the Spectral Behaviour of the Martian Surface, Nature, Vol. 22, 1969, pp. 132-136.

123. Younkin, R. L.: A Search for Limonite Near-Infrared Spectral Features on Mars, Astrophys. J., Vol. 144, 1966, pp. 809-818.

124. Tull, R. G.: The Reflectivity Spectrum of Mars in the Near Infrared, Icarus, Vol. 5, 1966, pp. 505-514.

125. Egan, W. G.: Polarimetric and Photometric Simulation of the Martian Surface, Icarus, Vol. 10, 1969, pp. 223-227.

126. Caldwell, J.: Ultraviolet Observations of Mars Made by the Orbiting Astronomical Observatory, Icarus, Vol. 18, 1973, pp. 489-496.

127. Sinton, W. M.: On the Composition of Martian Surface Materials, Icarus, Vol. 6, 1967, pp. 222-228.

128. Hunt, G. R.; Logan, L. M.; and Salisburg, J. W.: Mars: Components of Infrared Spectra and the Composition of the Dust Cloud, Icarus, Vol. 18, 1973, pp. 459-469.

129. Campbell, M. J., and Ulrichs, J.: Electrical Properties of Rocks and Their Significance for Lunar Radar Observations, JGR, Vol. 74, No. 25, 1969, pp. 5867-5881.

130. Morgan, S. O.; Edelson, D.; and McMahon, W.: Properties of Dielectrics, American Institute of Physics Handbook, McGraw-Hill, 2nd Ed., 1963, pp. 5-107 to 5-137.

131. Keller, G. V.: Electrical Properties of Rocks and Minerals, Section 20, Handbook of Physical Constants, edited by S. P. Clark, Jr., The Geol. Soc. of Amer., New York, 1966, pp. 55 -577.

132. Minnaert, M.: Photometry of the Moon, Planets and Satellites, The Solar System, Vol. III, edited by C. P. Kuiper and B. M. Middlehurst, University of Chicago Press, 1961.

133. de Vaucouleurs, G.: Geometric and Photometric Parameters of the Terrestrial Planets, Icarus, Vol. 3, 1964, pp. 187-235.

134. Russell, H. N.: On the Albedo of the Planets and Their Satellites, The Astrophys. J., Vol. 18, 1916, pp. 173-196.

135. Loomis, A. A.: Some Geologic Problems of Mars, Geol. Soc. Amer. Bull. 76, 1965, pp. 1083-1104.

136. Evans, D. C.: Ultraviolet Reflectivity of Mars, Science, Vol. 149, 1965, pp. 969-972.

137. McCord, T. B.; Ellis, J. H.; and Westphal, J. A.: Mars: The Spectral Albedo (0.3-2.5 μ) of Small Bright and Dark Regions, Icarus, Vol. 14, 1971, pp. 245-251.

138. Meador, W. E., and Weaver, W. R.: A Proposed Photometric Function for Diffuse Reflection by Particulate Materials. NASA TND 7903, March 1975.

139. Weaver, W. R.; Wood, G. P.; and Meador, W. E.: Values of Photometric Parameters of Mars and Their Interpretation. NASA-TM X-71949, May 1974.

140. Thorpe, T. E.: Mariner 9 Photometric Observations of Mars from November 1971 through March 1972, Icarus, Vol. 20, No. 4, December 1973, pp. 482-489.

141. Terzaghi, K., and Peck, R.: Soil Mechanics in Engineering Practice, J. Wiley and Sons, New York, 1967.

142. Anon.: Models of Mars' Atmosphere (1974), NASA SP-8010, revised December 1974.

APPENDIX A

SYMBOLS

A	Bond albedo (dimensionless)
A,B,C	semi-major axes of ellipsoids defining Martian geoid
A_{bol}	bolometric albedo (dimensionless)
B	observed radiance of the surface (cd/m^2)
B_o	radiance of a white screen parallel with the surface (cd/m^2)
B_n	radiance of a white screen oriented normal to incident rays (cd/m^2)
c	cohesion of soil (N/cm^2), or specific heat (cal/gK)
D	block or crater diameter (m)
e	emission angle, Figure 18, (deg)
E	solar constant ($cal/cm^2/min$)
E_S	solar luminosity constant (lm/m^2)
f	surface wave frequency (cycles/m), or dynamical flattening (dimensionless)
g	gravitational acceleration (m/s^2), or the photometric function parameter (dimensionless)
i	incidence angle, Figure 18, (deg) or the mathematical quantity $\sqrt{}$
I	thermal inertia ($cal/cm^2\ s^{1/2}K$)
k	thermal conductivity ($W/cm \cdot K$), or coefficient in cumulative crater frequency equation ($number/m^2$)
L	Martian surface base length (m)
L_S	heliocentric longitude (deg)
n	exponent in cumulative crater frequency equation (dimensionless)
N	fraction of surface slopes steeper than angle α

N_o	cumulative frequency distribution of blocks or craters larger than diameter D (number/square meter)
$P(\alpha)$	slope frequency probability density function (dimensionless)
R	planet radius (m)
R_E	planet mean equatorial radius (m)
T	surface temperature (K)
T_E	equatorial brightness temperature (K)
U	gravitational potential function (km^2/s^2)
V_*	surface wind drag velocity defined by Bagnold in Reference 59 (m/s)
V_t	minimum velocity to initiate motion of particles on the surface, Bagnold parameter (m/s)
α	local Martian slope (deg) or, phase angle in Figure 18 (deg)
$\bar{\alpha}$	mean Martian slope (deg)
β	latitude (deg)
γ	unit magnetic field (dimensionless), or optical thickness (dimensionless)
δ	angle in Figure 18 (deg)
tan δ	loss tangent (dimensionless)
ϵ	dielectric constant (dimensionless), or emissivity (dimensionless)
ϵ'	real part of dielectric constant (dimensionless)
ϵ''	imaginary part of dielectric constant (dimensionless)
θ	longitude of X axis which has a semi-major axis A (deg)
λ	wavelength (meters), or selenographic longitude (deg)
σ	Stefan-Boltzmann constant = 5.74×10^{-8} $W/m^2 \cdot K^4$, or standard deviation of slope frequency distribution (deg)
ρ	soil density (g/cm^3) or, radiance factor (dimensionless)

ρ_o	normal albedo (dimensionless)
ϕ	latitude (deg), soil friction angle (deg), or angle in Figure 18 (deg)
$\Phi(i,e,\alpha;\lambda)$	photometric function (dimensionless)
μ	selenographic latitude (deg) or gravitational constant, GM (km^3/s^2)
ψ	angle in Figure 18 (deg)

APPENDIX B

SHORT TABLE OF CONVERSION FACTORS

Multiply	By	To Obtain
m	3.281	ft
micrometer (μm)	3.281×10^{-6}	ft
angstrom (Å)	10^{-10}	m
km/s	3281	ft/s
m/s^2	3.281	ft/s^2
cycles/m	0.3048	cycles/ft
m^3/cycle	35.32	ft^3/cycle
g/cm^3	1.940	$slugs/ft^3$
newton (N)	0.2248	lbf
N/cm^2	1.451	lbf/in^2
mb	0.01451	lbf/in^2
N/cm^3	3.687	lbf/in^3
joules (J)	0.95×10^{-3}	BTU
watts (W)	0.95×10^{-3}	BTU/s
watts (W)	1.00	joules/s
cal	4.184	joules

APPENDIX C
GLOSSARY

Angstrom, Å – A unit used to express the wavelength of light ($1 Å = 10^{-10} m$).

Annual – Refers to the variation of a parameter during one revolution of the planet (yearly variation).

AU – Astronomical Unit, a distance equal to the average distance from the Sun to the Earth (1.495979×10^8 km).

Blackbody – An ideal body which is in complete thermodynamic equilibrium with its surroundings and radiates energy according to Planck's law.

Bolometric albedo – The bond albedo weighted over wavelengths by the solar flux (ref. 19).

Bond albedo – A measure of the reflectivity of a planet. It is the ratio of the total amount of sunlight reflected from the body in all directions to the amount falling upon the body.

Brightness temperature – The temperature of a blackbody that gives off the same radiant power at the particular wavelength as computed from the Planck equation.

Cohesion – A term used in soil mechanics to express the attractive force per unit area between soil grains.

Dielectric constant – The ratio of the permittivity (ϵ) of a material to the free space value (ϵ_0). This ratio is normally referred to as the relative or effective dielectric constant.

Diurnal – Refers to the variation of a parameter during one rotation of the planet (daily variation).

Flattening, f – A measure of the shape of a planet. Flattening is the difference between the mean equatorial diameter and polar diameter divided by the mean equatorial diameter.

Geometric albedo – The brightness of the surface divided by the brightness of a Lambert surface having the same inclination as the surface.

Heliocentric longitude – The angle to the planet as measured from the point in orbit where the Sun is in the zenith and moving northward, i.e., the beginning of spring in the Northern Hemisphere (see ref. 19).

Isophote – A line of equal or constant brightness.

Lambert surface – A surface which emits luminance flux at a rate proportional to the cosine of the angle between the surface normal and the direction of observation.

Loss tangent – The capacity of a material to transmit an electromagnetic wave. Transmission distance increases with a decreasing value of the loss tangent.

Luminance longitude – The angle of observation projected onto the phase plane, see Figure 18.

Millibar, mb – A unit of atmospheric pressure (1 bar = 10^6 dynes/cm^2)

Normal albedo – The brightness of the surface divided by the brightness of a Lambert surface (white screen) when observer and illuminator are located along the same normal vector.

Photoclinometry – The process of relating the measured brightness seen in a photograph to the viewing and lighting geometry, and the surface photometric function to obtain slope information.

Photometric function – The function relating reflectance properties of the surface to the viewing direction, solar illumination direction, and surface orientation.

Polarized light – A light beam in which the waves are all vibrating in a single plane.

Power spectral density (PSD) – A mathematical description of surface roughness expressed in terms of the mean square heights and lengths of a continuous distribution of harmonic surface undulations.

Radiance factor – Ratio of observed radiance of a point on the surface to the radiance of a white screen placed normal to the incident solar rays.

Relief – Total vertical rise of a surface feature, e.g., bottom of crater to top of rim.

Revolution – The orbital motion of a planet aound the Sun.

Rim height – Height of crater rim above local surface plane.

Rotation – The turning of a planet on its axis.

Seeing – A term used by astronomers to describe the visual appearance of a star of planet as affected by atmospheric conditions.

Solar Constant – The amount of radiant energy received from the Sun at the upper limits of the planet's atmosphere per unit time and unit surface area. (The solar "constant" actually varies slightly with time. Values quoted are estimates of the average value over the time interval of interest.)

Steradian – Solid angle subtended at the center of a sphere by an area on the surface equal to the square of the radius of the sphere. (The total solid angle about a point is 4π steradians.)

Subsolar point – The point on Mars where the Sun is at the zenith.

Terminator – The line that separates the illuminated and unilluminated portions of a planet.

Thermal inertia – A measure of the resistivity or resistance of a material to a change in temperature.

Thermal parameter – The inverse of the thermal inertia.

Triple point – A point on the pressure-temperature phase diagram of a substance in which solid, liquid and vapor phases may all three co-exist in equilibrium with one another.

NASA SPACE VEHICLE DESIGN CRITERIA MONOGRAPHS

ENVIRONMENT

SP-8005	Solar Electromagnetic Radiation, revised May 1971
SP-8010	Models of Mars' Atmosphere (1974) revised December 1974
SP-8011	Models of Venus Atmosphere (1972), revised September 1972
SP-8013	Meteoroid Environment Model–1969 (Near Earth to Lunar Surface), March 1969
SP-8017	Magnetic Fields–Earth and Extraterrestrial, March 1969
SP-8020	Surface Models of Mars (1975), revised September 1975
SP-8021	Models of Earth's Atmosphere (90 to 2500 km), revised March 1973
SP-8023	Lunar Surface Models, May 1969
SP-8037	Assessment and Control of Spacecraft Magnetic Fields, September 1970
SP-8038	Meteoroid Environment Model–1970 (Interplanetary and Planetary), October 1970
SP-8049	The Earth's Ionosphere, March 1971
SP-8067	Earth Albedo and Emitted Radiation, July 1971
SP-8069	The Planet Jupiter (1970), December 1971
SP-8084	Surface Atmospheric Extremes (Launch and Transportation Areas), revised June 1974
SP-8085	The Planet Mercury (1971), March 1972
SP-8091	The Planet Saturn (1970), June 1972
SP-8092	Assessment and Control of Spacecraft Electromagnetic Interference, June 1972
SP-8103	The Planets Uranus, Nepture, and Pluto (1971), November 1972

SP-8105	Spacecraft Thermal Control, May 1973
SP-8111	Assessment and Control of Electrostatic Charges, May 1974
SP-8116	The Earth's Trapped Radiation Belts, March, 1975
SP-8117	Gravity Fields of the Solar System, April 1975
SP-8118	Interplanetary Charged Particle Models (1974), March 1975

STRUCTURES

SP-9011	Buffeting During Atmospheric Ascent, revised November 1970
SP-8002	Flight-Loads Measurements During Launch and Exit, revised June 1972
SP-8003	Flutter, Buzz, and Divergence, July 1964
SP-8004	Panel Flutter, revised June 1972
SP-8006	Local Steady Aerodynamic Loads During Launch and Exit, May 1965
SP-8007	Buckling of Thin-Walled Circular Cylinders, revised August 1968
SP-8008	Prelaunch Ground Wind Loads, November 1965
SP-8009	Propellant Slosh Loads, August 1968
SP-8012	Natural Vibration Modal Analysis, September 1968
SP-8014	Entry Thermal Protection, August 1968
SP-8019	Buckling of Thin-Walled Truncated Cones, September 1968
SP-8022	Staging Loads, February 1969
SP-8029	Aerodynamic and Rocket-Exhaust Heating During Launch and Ascent, May 1969
SP-8031	Slosh Suppression, May 1969
SP-8032	Buckling of Thin-Walled Doubly Curved Shells, August 1969
SP-8035	Wind Loads During Ascent, June 1970
SP-8040	Fracture Control of Metallic Pressure Vessels, May 1970

SP-8042	Meteoroid Damage Assessment, May 1970
SP8043	Design–Development testing, May 1970
SP-8044	Qualification testing, May 1970
SP-8045	Acceptance testing, April 1970
SP-8046	Landing Impact Attenuation for Non-Surface-Planning Landers, April 1970
SP-8050	Structural Vibration Prediction, June 1970
SP-8053	Nuclear and Space Radiation Effects on Materials, June 1970
SP-8054	Space Radiation Protection, June 1970
SP-8055	Prevention of Coupled Structure-Propulsion Instability (Pogo), October 1970
SP-8056	Flight Separation Mechanisms, October 1970
SP-8057	Structural Design Criteria Applicable to a Space Shuttle, revised March 1972
SP-8060	Compartment Venting, November 1970
SP-8061	Interaction with Umblicals and Launch Stand, August 1970
SP-8062	Entry Gasdynamic Heating, January 1971
SP-8063	Lubrication, Friction, and Wear, June 1971
SP-8066	Deployable Aerodynamic Deceleration Systems, June 1971
SP-8068	Buckling Strength of Structural Plates, June 1971
SP-8072	Acoustic Loads Generated by the Propulsion System, June 1971
SP-8077	Transportation and Handling Loads, September 1971
SP-8079	Structural Interaction with Control Systems, November 1971
SP-8082	Stress-Corrosion Cracking in Metals, August 1971
SP-8083	Discontinuity in Metallic Pressure Vessels, November 1971

SP-8095	Preliminary Criteria for the Fracture Control of Space Shuttle Structures, June 1971
SP-8099	Combining Ascent Loads, May 1972

GUIDANCE AND CONTROL

SP-8015	Guidance and Navigation for Entry Vehicles, November 1968
SP-8016	Effects of Structural Flexibility on Spacecraft Control Systems, April 1969
SP-8018	Spacecraft Magnetic Torques, March 1969
SP-8024	Spacecraft Gravitational Torques, May 1969
SP-8026	Spacecraft Star Trackers, July 1970
SP 8027	Spacecraft Radiation Torques, October 1969
SP-8028	Entry Vehicle Control, November 1969
SP-8033	Spacecraft Earth Horizon Sensors, December 1969
SP-8034	Spacecraft Mass Expulsion Torques, December 1969
SP-8036	Effects of Structural Flexibility on Launch Vehicle Control Systems, February 1970
SP-8047	Spacecraft Sun Sensors, June 1970
SP-8058	Spacecraft Aerodynamic Torques, January 1971
SP-8059	Spacecraft Attitude Control During Thrusting Maneuvers, February 1971
SP-8065	Tubular Spacecraft Booms (Extendible, Reel Stored), February 1971
SP-8070	Spaceborne Digital Computer Systems, March 1971
SP-8071	Passive Gravity-Gradient Libration Dampers, February 1971
SP-8074	Spacecraft Solar Cell Arrays, May 1971
SP-8078	Spaceborne Electronic Imaging Systems, June 1971
SP-8086	Space Vehicle Displays Design Criteria, March 1972

SP-8098 Effects of Structural Flexibility on Entry Vehicle Control Systems, June 1972

SP-8102 Space Vehicle Accelerometer Applications, December 1972

CHEMICAL PROPULSION

SP-8025 Solid Rocket Motor Metal Cases, April 1970

SP-8039 Solid Rocket Motor Performance Analysis and Prediction, May 1971

SP-8041 Captive-Fired Testing of Solid Rocket Motors, March 1971

SP-8048 Liquid Rocket Engine Turbopump Bearings, March 1971

SP-8051 Solid Rocket Motor Igniters, March 1971

SP-8052 Liquid Rocket Engine Turbopump Inducers, May 1971

SP-8064 Solid Propellant Selection and Characterization, June 1971

SP-8073 Solid Propellant Grain Structural Integrity Analysis, June 1973

SP-8075 Solid Propellant Processing Factors in Rocket Motor Design, October 1971

SP-8076 Solid Propellant Grain Design and Internal Ballistics, March 1972

SP-8080 Liquid Rocket Pressure Regulators, Relief Valves, Check Valves, Burst Disks, and Explosive Valves, March 1973

SP-8081 Liquid Propellant Gas Generators, March 1972

SP-8087 Liquid Rocket Engine Fluid-Cooled Combustion Chambers, April 1972

SP-8088 Liquid Rocket Metal Tanks and Tank Components, May 1974

SP-8090 Liquid Rocket Actuators and Operators, May 1973

SP-8094 Liquid Rocket Valve Components, August 1973

SP-8097 Liquid Rocket Valve Assemblies, November 1973

SP-8100 Liquid Rocket Engine Turbopump Gears, March 1974

SP-8101 Liquid Rocket Engine Turbopump Shafts and Couplings, September 1972

SP-8110 Liquid Rocket Engine Turbines, January 1974